



Massive Protostars in a Protocluster—A Multi-scale ALMA View of G35.20-0.74N

Yichen Zhang^{1,2} , Kei E. I. Tanaka^{3,4} , Jonathan C. Tan^{1,5} , Yao-Lun Yang^{1,2} , Eva Greco¹, Maria T. Beltrán⁶ , Nami Sakai² , James M. De Buizer⁷ , Viviana Rosero⁸ , Rubén Fedriani⁵ , and Guido Garay⁹

¹Department of Astronomy, University of Virginia, Charlottesville, VA 22904-4325, USA; yczhang.astro@gmail.com

²Star and Planet Formation Laboratory, RIKEN Cluster for Pioneering Research, Wako, Saitama 351-0198, Japan

³Center for Astrophysics and Space Astronomy, University of Colorado Boulder, Boulder, CO 80309, USA

⁴ALMA Project, National Astronomical Observatory of Japan, Mitaka, Tokyo 181-8588, Japan

⁵Department of Space, Earth & Environment, Chalmers University of Technology, SE-412 96 Gothenburg, Sweden

⁶INAF—Osservatorio Astrofisico di Arcetri, Largo E. Fermi 5, I-50125 Firenze, Italy

⁷SOFIA-USRA, NASA Ames Research Center, MS 232-12, Moffett Field, CA 94035, USA

⁸National Radio Astronomy Observatory, 1003 Lopezville Road, Socorro, NM 87801, USA

⁹Departamento de Astronomía, Universidad de Chile, Casilla 36-D, Santiago, Chile

Received 2021 December 13; revised 2022 July 19; accepted 2022 July 22; published 2022 August 31

Abstract

We present a detailed study of the massive star-forming region G35.2-0.74N with Atacama Large Millimeter/submillimeter Array (ALMA) 1.3 mm multi-configuration observations. At $0''.2$ (440 au) resolution, the continuum emission reveals several dense cores along a filamentary structure, consistent with previous ALMA 0.85 mm observations. At $0''.03$ (66 au) resolution, we detect 22 compact sources, most of which are associated with the filament. Four of the sources are associated with compact centimeter continuum emission, and two of these are associated with H30 α recombination line emission. The H30 α line kinematics shows the ordered motion of the ionized gas, consistent with disk rotation and/or outflow expansion. We construct models of photoionized regions to simultaneously fit the multiwavelength free-free fluxes and the H30 α total fluxes. The derived properties suggest the presence of at least three massive young stars with nascent hypercompact H II regions. Two of these ionized regions are surrounded by a large rotating structure that feeds two individual disks, revealed by dense gas tracers, such as SO₂, H₂CO, and CH₃OH. In particular, the SO₂ emission highlights two spiral structures in one of the disks and probes the faster-rotating inner disks. The ¹²CO emission from the general region reveals a complex outflow structure, with at least four outflows identified. The remaining 18 compact sources are expected to be associated with lower-mass protostars forming in the vicinity of the massive stars. We find potential evidence for disk disruption due to dynamic interactions in the inner region of this protocluster. The spatial distribution of the sources suggests a smooth overall radial density gradient without subclustering, but with tentative evidence of primordial mass segregation.

Unified Astronomy Thesaurus concepts: Star forming regions (1565); Massive stars (732); Stellar accretion disks (1579); Protostars (1302); H II regions (694)

1. Introduction

Massive stars dominate the radiative, mechanical, and chemical feedback to the interstellar medium, by which they regulate the evolution of galaxies. Their feedback also affects nearby low-mass forming stars and their protoplanetary disks. In spite of their importance, many aspects of massive star formation remain poorly understood (see, e.g., Tan et al. 2014; Motte et al. 2018).

One of the challenges to form a massive star is its strong feedback on its natal gas core. In particular, protostellar extreme-ultraviolet radiation can ionize the accretion disk and infall envelope to produce photoevaporative outflows driven by the thermal pressure of the $\sim 10^4$ K ionized gas (Hollenbach et al. 1994). Detection of a H II region via free-free continuum emission and/or hydrogen recombination lines (HRLs) has traditionally been considered as an indication of the end of the accretion phase (e.g., Churchwell 2002). However, theoretical calculations have suggested that such feedback may not be strong enough to stop accretion (e.g., Keto 2002; Peters et al. 2010; Tanaka et al. 2017;

Kuiper & Hosokawa 2018), and recent high-resolution observations have revealed cases of ongoing accretion after the onset of photoionization (e.g., Zhang et al. 2019c; Maud et al. 2019; Guzman et al. 2020; Moscadelli et al. 2021). Understanding the accretion status after the onset of photoionization is therefore crucial to constrain the growing efficiency under feedback during the later stages of the birth of massive stars.

Another important question is how accretion proceeds in massive star formation. There are a growing number of examples of accretion disks around massive protostars (e.g., Sánchez-Monge et al. 2013; Johnston et al. 2015; Ilee et al. 2016; Ginsburg et al. 2018; Maud et al. 2018; Zhang et al. 2019b; Tanaka et al. 2020; see also Beltrán & de Wit 2016 and references therein), suggesting that disk-mediated accretion is common during massive star formation. On the other hand, there are also some examples of massive young stars in which the accretion appears to occur without mediation from a large, stable disk, but rather from multiple, more chaotic flows (e.g., Goddi et al. 2020). Disks around massive protostars may be prone to gravitational instability and thus relatively likely to fragment and form binaries or close multiple systems. However, direct observations of substructures in massive protostellar disks are rare (e.g., Motogi et al. 2019; Johnston et al. 2020). Massive protostellar binary systems with a few



Original content from this work may be used under the terms of the [Creative Commons Attribution 4.0 licence](https://creativecommons.org/licenses/by/4.0/). Any further distribution of this work must maintain attribution to the author(s) and the title of the work, journal citation and DOI.

hundreds of au separations have been speculated to be the result of such disk fragmentation, with continued accretion mediated by a circumbinary accretion disk or pseudo-disk (e.g., Beltrán et al. 2016; Kraus et al. 2017; Zhang et al. 2019a), although the morphology of such a circumbinary accretion structure may have evolved significantly after binary formation (e.g., Tanaka et al. 2020). Therefore, detailed, multi-scale observations of the hierarchical structures of the accretion flows around massive protostars are important to understand the global accretion process involved in massive star formation.

On larger scales ($\gtrsim 0.01$ pc), the fragmentation of the molecular clump leads to the formation of a cluster with both low- and high-mass stars (see, e.g., Motte et al. 2018). The degree of fragmentation is found to be diverse among different massive star-forming regions (e.g., Palau et al. 2013; Beuther et al. 2018), which is expected to be affected by various factors such as the initial density distribution, magnetic field strength, degree of turbulence, and radiative heating of the cloud. The distributions of the massive stars within the cluster and the spatial separations of the members can provide important information on the fragmentation mechanism and help distinguish if massive stars form via core accretion (e.g., McKee & Tan 2003) or competitive accretion (e.g., Bonnell et al. 2001; Wang et al. 2010). For example, Bonnell & Davies (1998) concluded massive stars formed preferentially in the center of the Orion Nebular Cluster. On the other hand, Moser et al. (2020) did not find strong evidence for primordial mass segregation in the massive protostar population of the massive Infrared Dark Cloud G028.37+00.07. Gravitational interactions and/or radiative and mechanical feedback from massive forming stars in crowded protocluster environments may also affect neighboring low-mass protostars and their disks. It is therefore important to perform detailed studies of massive star formation in the context of star cluster formation.

G35.20-0.74N (a.k.a. IRAS 18566+0136; hereafter G35.2) is an ideal target to study all these processes to understand the formation of massive stars. It is a well-known massive star-forming region at a distance of 2.2 kpc (Zhang et al. 2009; Wu et al. 2014). Previous observations of the Atacama Large Millimeter/submillimeter Array (ALMA) and the Submillimeter Array (SMA) have revealed a filamentary structure with a string of embedded cores (Qiu et al. 2013; Sánchez-Monge et al. 2013, 2014). CO observations have revealed a wide outflow structure extending to $>1'$ from the central source (Gibb et al. 2003; Birks et al. 2006) in the direction of the northeast–southwest (NE–SW), which is near perpendicular to the filament. Consistent with this wide CO outflow, near-infrared (NIR) H_2 observations also show a wide outflow structure in the NE–SW direction, which may contain two outflows (Caratti o Garatii et al. 2015). On the other hand, centimeter radio observations of the Very Large Array (VLA) have revealed a collimated bipolar ionized jet along the north–south (N–S) direction (Heaton & Little 1988; Gibb et al. 2003; Beltrán et al. 2016), with its driving source being one of the sub-mm cores of the filament (core B, Sánchez-Monge et al. 2013, 2014; Beltrán et al. 2016). Fedriani et al. (2019) revealed NIR emission spatially coincident with the radio jet in the central region. This N–S outflow is also prominent in mid-infrared (MIR; De Buizer 2006). At these wavelengths, the emission is elongated in the N–S direction but peaked to the north of the identified radio source and continuum core and is thought to trace the blueshifted outflow cavity. At longer

wavelengths of 30–40 μm , the SOFIA-FORCAST observations have revealed the southern, far-facing outflow cavity (Zhang et al. 2013; De Buizer et al. 2017). The driving source of the N–S outflow (core B) is reported to have a Keplerian accretion disk (Sánchez-Monge et al. 2013), with the dynamical mass estimated to be about $18 M_\odot$. Beltrán et al. (2016) further identified a binary system in core B (VLA sources 8a and 8b). By fitting the infrared spectral energy distribution (SED) assuming a single protostar, core B is estimated to be a protostar with a mass of $12\text{--}24 M_\odot$ and a total luminosity of $(4\text{--}8) \times 10^4 L_\odot$ (Zhang et al. 2013; De Buizer et al. 2017; Zhang & Tan 2018). In this paper, we present a detailed study of G35.20-0.74N using multiwavelength continuum, molecular line, and HRL data obtained by ALMA and VLA.

2. Observations

The observations were carried out with ALMA in Band 6 (1.3 mm) on 2016 April 24 with the C36-3 (hereafter C3) configuration, on 2016 September 8 with the C36-6 (hereafter C6) configuration, and on 2017 November 4 with the C43-9 (hereafter C9) configuration (ALMA project ID: 2015.1.01454.S and 2017.1.00181.S). The total integration times are 3.5, 6.5, and 16.8 minutes in the three configurations. Forty-one antennas were used with baselines ranging from 15–463 m in the C3 configuration, 38 antennas were used with baselines ranging from 15 m to 2.5 km in the C6 configuration, and 49 antennas were used with baselines ranging from 113 m to 13.9 km in the C9 configuration. J1751+0939, J1924-2914, and J2000-1748 were used for bandpass calibration and flux calibration. J1830+0619 and J1851+0035 were used as phase calibrators. The science target was observed with single pointings, and the primary beam size (half power beamwidth) was $22''.9$.

The data were calibrated and imaged in CASA (McMullin et al. 2007). After pipeline calibration, we performed self-calibration using the continuum data obtained from a 2 GHz-wide spectral window with line-free bandwidth of 1.2 GHz. We first performed two phase-only self-calibration iterations with solution intervals of 30 and 6 s, and then one iteration of amplitude self-calibration with the solution interval equal to the scan intervals (ranging from ~ 1 to ~ 5 minutes). We applied the self-calibration phase and amplitude solutions to the other spectral windows. Such self-calibration was performed for the data of three configurations separately before any combining was performed. The CASA *tclean* task was used to image the data, using Briggs weighting with the robust parameter set to 0.5. In order to better show structures on different scales, below we present images made of different configuration combinations. The resolution of the C3+C6 configuration is about $0''.25$, and the resolution of the image of just the C9 configuration is about $0''.03$, the highest achieved so far for this region at millimeter wavelengths. Detailed synthesized beam sizes of images of different configuration combinations, as well as their rms noise levels, are listed in Table 1.

We also utilize the ALMA Band 7 (0.85 mm) continuum data published by Sánchez-Monge et al. (2013). Please refer to that paper for details of the observation. Instead of directly using the published 0.85 mm continuum image, we reproduced the continuum image using the calibrated data obtained from the ALMA archive. From the four 2 GHz wide spectral windows, we imaged the continuum emission using line-free channels, which span a total of 0.86 GHz. We performed two

Table 1
Properties of the Presented Continuum Images

Telescope	Band	Wavelength (mm)	Configuration	Synthesized Beam	Noise rms mJy beam ⁻¹	Noise rms K
ALMA	Band 7 ^a	0.85	Extended (cycle 0)	0".47 × 0".42 (P. A. = 51°4)	0.73	0.039
ALMA	Band 6	1.3	C3+C6	0".25 × 0".25 (P. A. = -36°3)	0.48	0.17
ALMA	Band 6	1.3	C3+C6+C9	0".045 × 0".033 (P. A. = -64°0)	0.085	1.3
ALMA	Band 6	1.3	C6+C9	0".043 × 0".031 (P. A. = -63°3)	0.088	1.5
ALMA	Band 6	1.3	C9	0".037 × 0".027 (P. A. = -66°0)	0.061	1.4
VLA	<i>Q</i> band ^b	7	A	0".046 × 0".036 (P. A. = -52°0)	0.020	7.7
VLA	<i>Q</i> band ^b	7	B	0".14 × 0".12 (P. A. = -44°5)	0.030	1.1
VLA	<i>Ku</i> band ^b	13	A	0".079 × 0".076 (P. A. = -46°3)	0.013	5.2
VLA	<i>Ku</i> band ^b	13	B	0".25 × 0".24 (P. A. = 39°5)	0.020	0.8

Notes.

^a Reimaged using the data published by Sánchez-Monge et al. (2013).

^b Beltrán et al. (2016).

phase-only self-calibration iterations with solution intervals of 30 and 6 s, and then one iteration of amplitude self-calibration with the solution interval equal to the scan intervals (ranging from ~1 to ~5 minutes). The CASA *tclean* task was used to image the data, using Briggs weighting with the robust parameter set to 0.5.

In addition, we also utilize the VLA *K*-band (1.3 cm) and *Q*-band (7 mm) continuum images published by Beltrán et al. (2016). See that paper for details of the VLA observations. The synthesized beams and noise levels of these images are also listed in Table 1.

3. Continuum Emission

3.1. Lower-resolution 1.3 mm Continuum

Panels (a) and (b) of Figure 1 show the ALMA 1.3 mm continuum image, combining the data of the C3 and C6 configurations, and the reproduced 0.85 mm continuum image. In general, the 1.3 mm continuum morphology is consistent with that of the 0.85 mm continuum, i.e., showing multiple cores along the filamentary structure. Compared to that presented by Sánchez-Monge et al. (2013), the new 0.85 mm continuum image shows a compact source to the west of core A (labeled as source 3 in the figure; see Section 3.2). This source is seen as a compact continuum source in the 1.3 mm continuum image, as well as all the VLA images, but was not seen in the previously presented 0.85 mm image. Detection of this source in the reproduced 0.85 mm continuum image is probably due to the improved sensitivity brought by the self-calibration. The new 0.85 mm image also shows more diffuse emission in the southern end of the filament, which is also seen in the 1.3 mm continuum image. Panel (c) shows a comparison between the 1.3 and 0.85 mm continuum. The overall morphology and the locations of the bright sources/regions coincide very well in the two images.

Figure 1(d) shows the spectral index map between ALMA 1.3 and 0.85 mm continuum. Here, the spectral index is defined as $\alpha_\nu = \log(I_{\nu_1}/I_{\nu_2})/\log(\nu_1/\nu_2)$, where I_ν is the intensity at the frequency ν , $\nu_1 = 343$ GHz (0.85 mm) and $\nu_2 = 234$ GHz (1.3 mm). The spectral index map is obtained with the 0.85 mm data and 1.3 mm C3+C6 data, using multifrequency synthesis (mtmfs) in the CASA *tclean* task with *nterms* = 2. In order to derive the spectral index map more accurately, we only used the 1.3 mm data with baselines between 20 and 440 k λ to match the *uv* range of the 0.85 mm data.

Typical dust continuum emission has spectral indices of $\alpha_\nu > 2$, with $\alpha_\nu = 2$ in the optically thick case and $3 \gtrsim \alpha_\nu \gtrsim 4$ in the optically thin case (assuming a typical dust emissivity spectral index of 1–2). Free–free continuum emission has spectral indices of $-0.1 \lesssim \alpha_\nu < 2$, with $\alpha_\nu = 2$ in the optically thick case and $\alpha_\nu \approx -0.1$ in the optically thin case. Cores A and B have spectral indices below 2, which suggests a contribution of free–free emission, expected for forming massive stars. However, the observed spectral indices are not far from 2. Optically thick dust emission or a combination of free–free and dust emission can also lead to such spectral indices. The regions with spectral indices above 2, which are dominated by dust emission, are mostly around cores A and B along the filament, suggesting dusty envelopes around the small H II regions created by the forming massive stars. Cores C, D, and F all have spectral indices close to 3, dominated by dust emissions, while core E has a spectral index slightly above 2, indicating a higher free–free fraction or high optical depth. Source 3 has a very flat SED between 1.3 and 0.85 mm, suggesting it is dominated by free–free emission.

3.2. Long-baseline 1.3 mm Continuum

Figure 2 shows the high-resolution view of the 1.3 mm continuum emission. From the long-baseline continuum data (C9 configuration), we are able to identify a total of 22 compact sources in the whole field of view with a primary beam response >0.1 (20 sources within the radius of primary beam response >0.5). The candidates of compact sources are first identified with maximum intensities $>5\sigma_{\text{noise}}$ ($1\sigma_{\text{noise}} = 0.06$ mJy beam⁻¹) and size estimated for regions with intensities $>4\sigma_{\text{noise}}$ larger than that of one beam size. We further removed the emission peaks caused by the extended filament emissions or the bright patches of the residual pattern, and made sure that the remaining compact sources clearly stand out from the residual pattern fluctuation. Note that the residual pattern close to the central region has a fluctuation level of $1\sigma_{\text{residual}} = 0.1$ mJy beam⁻¹. And the confirmed compact sources all have peaks $\gtrsim 6\sigma_{\text{residual}}$ ($\gtrsim 10\sigma_{\text{noise}}$). Figure 3 shows the continuum image of each source. Table 2 lists the identified compact sources, as well as their associated cores and corresponding VLA compact sources. The positions of these sources are also marked in panels (a) and (b) of Figure 1 to show their association with the larger-scale structures.

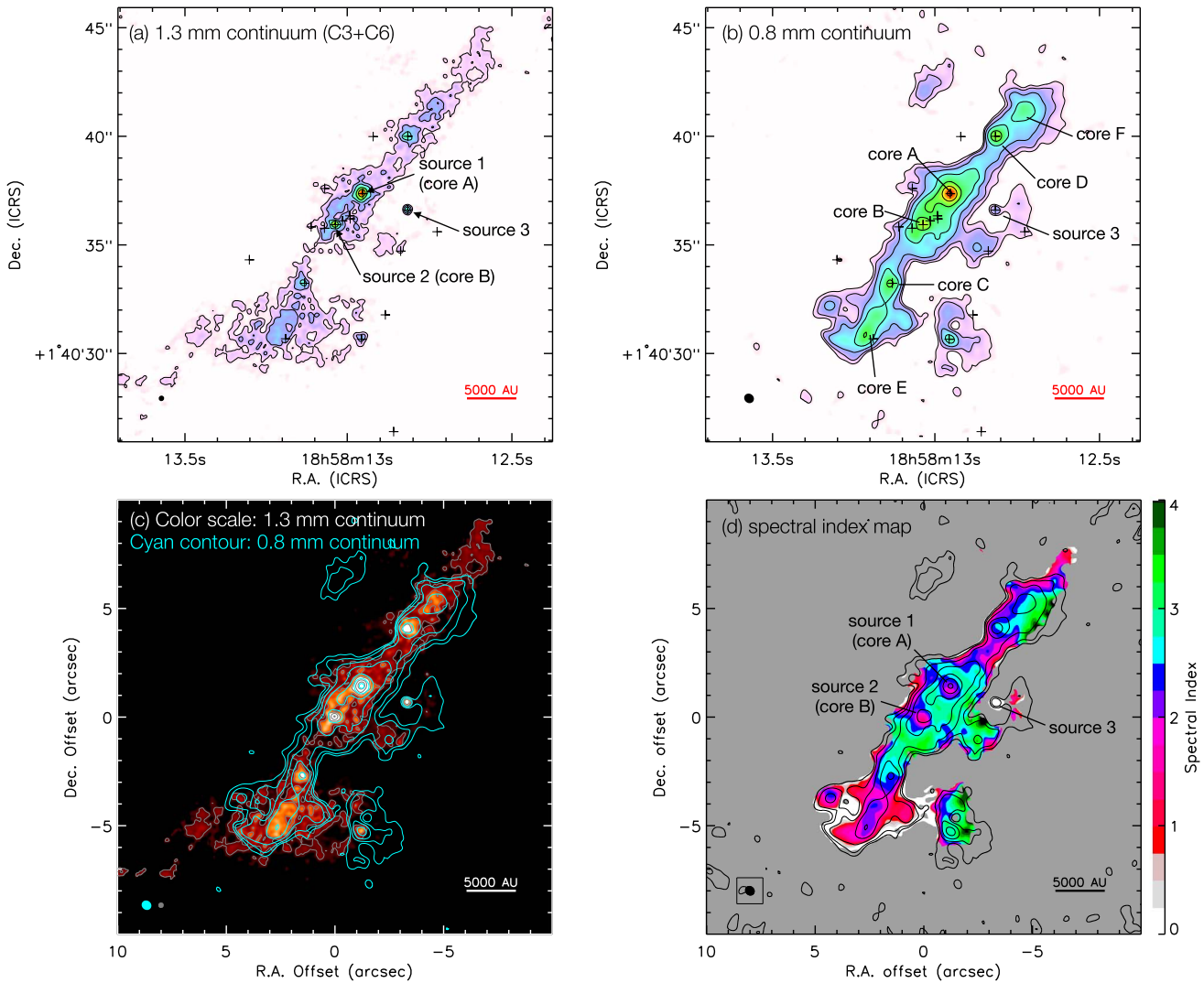


Figure 1. (a) Lower-resolution ALMA 1.3 mm (Band 6) continuum image of the G35.2 star-forming region, obtained by combining data from the C3 and C6 configurations. The contour levels are $5\sigma \times 2^n$ ($n = 0, 1, \dots$), with $1\sigma = 0.17$ K (0.48 mJy beam $^{-1}$) the synthesized beam is $0''.254 \times 0''.250$ (P. A. = $-36^\circ 3$). The crosses mark the position of the compact sources identified from a high-resolution 1.3 mm continuum image and the names of the three main sources are labeled (see Figure 2 and Table 2). (b) The 0.85 mm continuum image was reimaged using the data published by Sánchez-Monge et al. (2014). The synthesized beam is $0''.47 \times 0''.42$ (P. A. = $51^\circ 4$) and contour levels of $5\sigma \times 2^n$ ($n = 0, 1, \dots$) with $1\sigma = 0.039$ K (0.74 mJy beam $^{-1}$). The cores A–F identified from the 0.85 mm image by Sánchez-Monge et al. (2014) are labeled. The crosses are the same as in panel (a). (c) Comparison of the ALMA 1.3 mm continuum image (color scale and gray contours) and the 0.85 mm continuum image (cyan contours). (d) Spectral index map between 1.3 and 0.85 mm shown in color scale, overlaid with the 1.3 mm continuum image with the same contour levels as in panel (a). The spectral index is defined as $\alpha_\nu = \log(I_{\nu_1}/I_{\nu_2})/\log(\nu_1/\nu_2)$, where $\nu_1 = 234$ GHz and $\nu_2 = 343$ GHz. Only the regions with $>10\sigma$ continuum emissions and spectral index errors <0.5 are shown in the figure. The origin of the R.A. and decl. offsets in panels (c) and (d) are set to be core B ($\alpha_{\text{ICRS}} = 18^{\text{h}}58^{\text{m}}13^{\text{s}}.037$, $\delta_{\text{ICRS}} = +1^\circ40'35''.931$).

Most of the compact continuum sources are along the filament, especially around cores A and B. Among the six cores previously identified from the lower-resolution 0.85 mm continuum image, five (except core F) have associated compact continuum sources. ALMA source 3, which is a bright and compact source in both the long-baseline and lower-resolution 1.3 mm images is now also shown in our new 0.85 mm continuum image (Figure 1(b)). ALMA source 16 is also seen to be associated with a dense core structure in the new 0.85 mm continuum, which was not reported previously.

Figure 4 overlays the VLA 1.3 and 7 mm continuum emission images in the B and A configurations with the 1.3 mm low- and high-resolution continuum images. As previously pointed out, the large-scale VLA continuum emission mostly traces a radio jet originating from core B (source 2 in our list). As can be seen in this figure, ALMA

sources 1–4 have associated emissions in the VLA bands. ALMA sources 2 and 4, which are associated with VLA sources 8a and 8b, respectively, are likely members of a binary system, as suggested by Beltrán et al. (2016).

ALMA sources 1–4 are the only four 1.3 mm compact sources associated with VLA compact emission (VLA sources 3, 8a, 1, and 8b). The other emission knots identified in the VLA continuum maps do not have any counterpart compact source at 1.3 mm. These sources mostly have flat or negative spectral indices in VLA bands (see Beltrán et al. 2016). Extrapolating from the VLA bands to ALMA 1.3 mm, their fluxes should be below the continuum detection limits of ALMA unless there are additional dust contributions. Therefore, the non-detection of these VLA sources in ALMA 1.3 mm supports the idea that they are jet knots caused by shock ionization and are not protostars (Beltrán et al. 2016). Such a

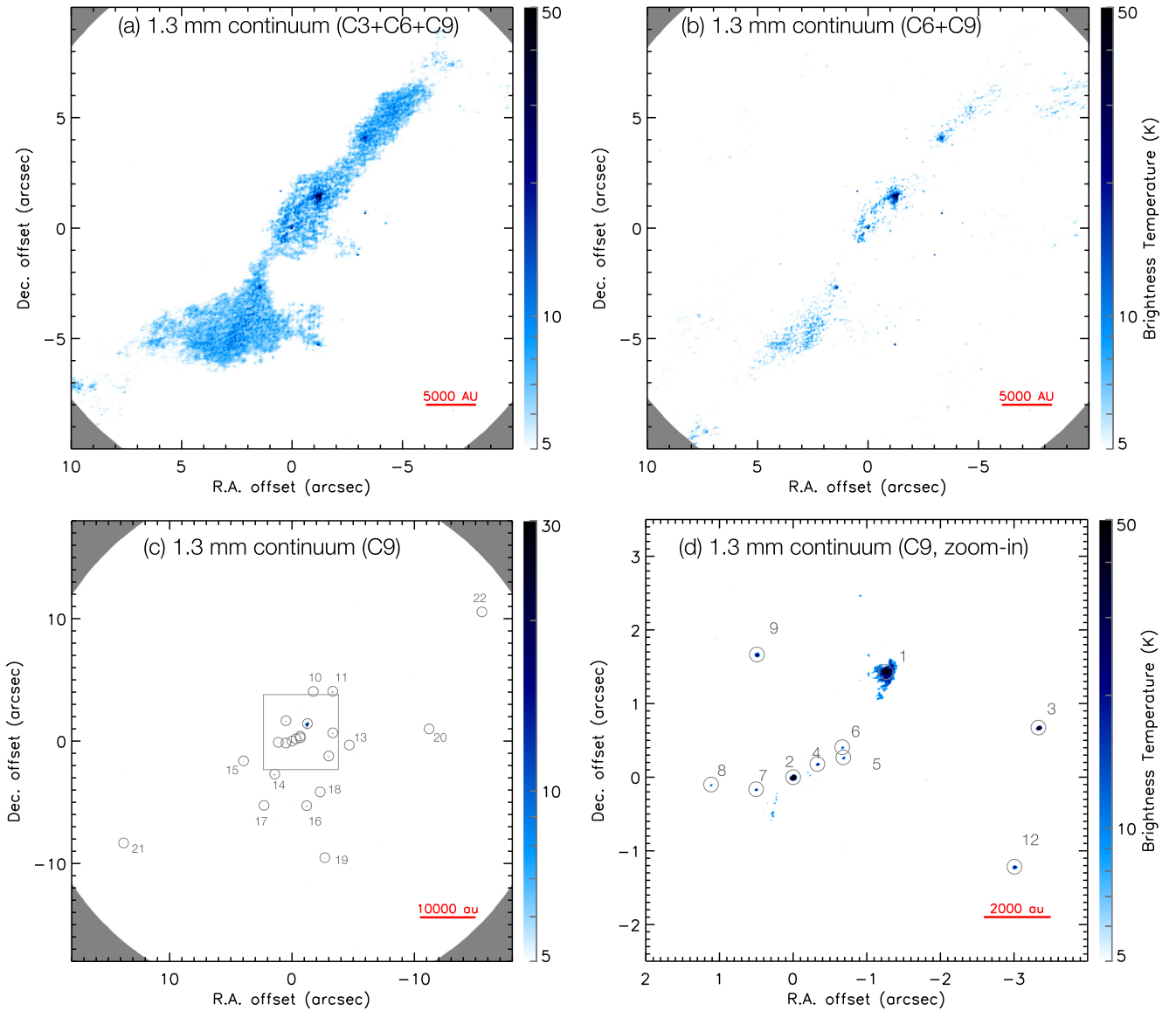


Figure 2. High-resolution ALMA 1.3 mm continuum images from different configurations. (a) Combined image from the C3, C6, and C9 configurations. (b) Combined image from C6 and C9 configurations. (c) Image from C9 configuration alone. (d) Same as panel (c), but zoomed in to the central region. The synthesized beam size of each image is listed in Table 1. The color scale (same for all the panels) is adjusted to emphasize the compact continuum sources. In panels (a) and (b), only the regions with a primary beam response of >0.5 are shown. In panel (c), all the regions with a primary beam response of >0.1 are shown. The identified compact continuum sources are marked with circles and labeled with numbers in panels (c) and (d).

scenario is also supported by the fact that Fedriani et al. (2019) detected atomic ($[\text{Fe II}]$ and $\text{Br}\gamma$) and molecular (H_2) emissions associated with shocks toward the north side of core B, i.e., the blueshifted outflow (also see Section 6.2). On the other hand, the other ALMA compact sources that are not detected in VLA bands (ALMA sources 5–22) should be lower-mass protostars (or relatively massive but young sources which have not yet reached the main sequence to produce detectable photoionized regions) forming along with the photoionizing massive stars.

For the ALMA sources with corresponding centimeter emission (sources 1–4), Figure 5 shows their continuum SEDs from 6 cm to 1.3 mm. The VLA flux densities are obtained from Beltrán et al. (2016). The 1.3 mm flux densities are obtained from the long-baseline (C9) data. These sources have spectral indices from 6 cm to 7 mm (VLA bands) either near flat (source 4) or slightly higher than 1 (sources 1–3), consistent with free-free emission. Free-free emission tends

to have its spectral index decrease as the frequency becomes higher. However, in all these sources, the spectral indices tend to increase at 1.3 mm (especially in sources 1 and 4), indicating dust contributions. As the free-free emission in these sources is highly compact, the different baseline ranges in these data have minimum effects on the SED slope. For the 1.3 mm data, we also only focus on the most compact emission structures here, so filtering out of the extended dust emission in the C9 configuration data does not affect our discussion. The compact dust emission confirms that they are forming stars rather than jet knots. For sources 1–3, the existence of bright free-free and dust emission is consistent with forming massive stars creating small ionized regions via photoionization. This was speculated by Beltrán et al. (2016) and is now further supported by the ALMA observations. For source 4, while such a scenario is also possible, it is 1.3 mm flux is on a similar level as the other low-mass sources in the

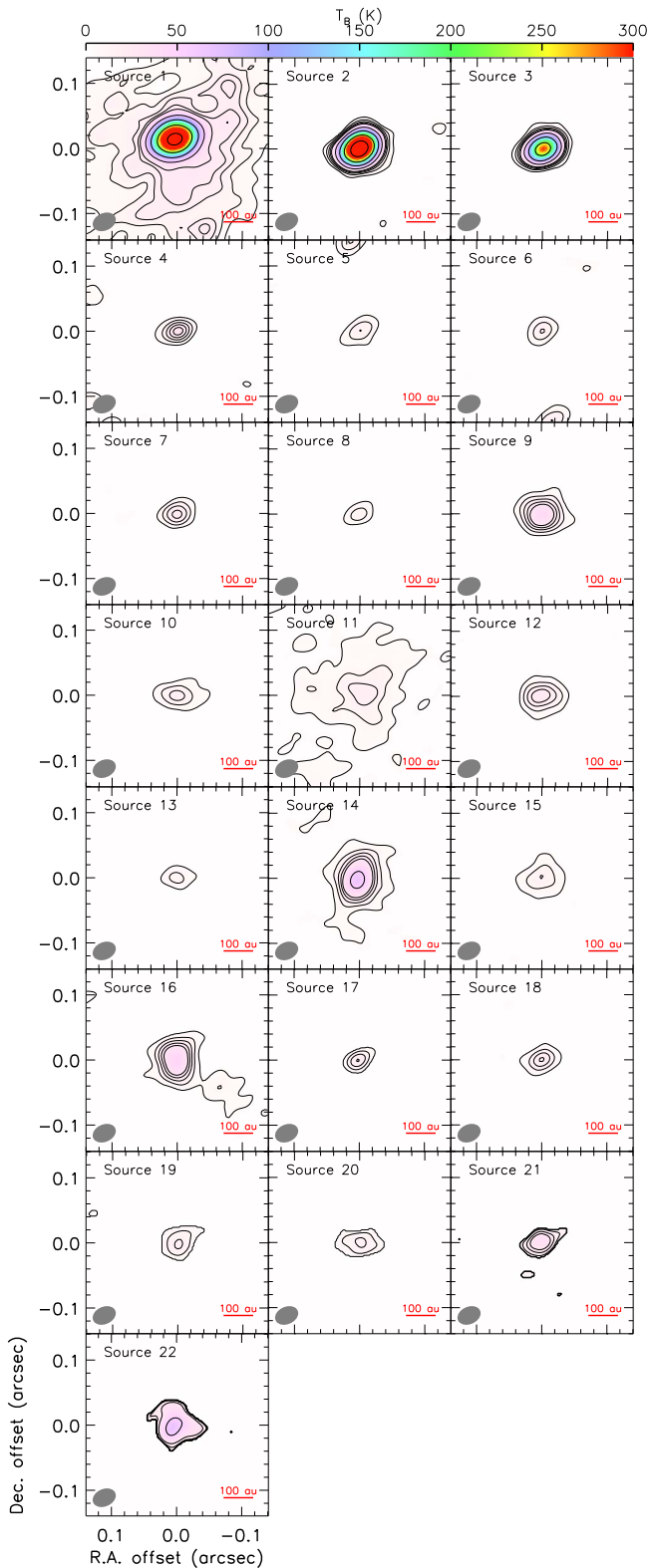


Figure 3. ALMA long-baseline 1.3 mm continuum images of all the compact sources identified (see Table 2). The contour levels are 4, 8, 12, 16, 20, 40, 80, 160, and 320 times the rms noise $1\sigma = 0.0608 \text{ mJy beam}^{-1}$ (1.37 K). The synthesized beam is shown in the bottom-left corner of each panel.

region. If source 4 is not yet massive enough to produce enough ionizing photons, the free-free emission could be caused by shock ionization of an unresolved jet, which is seen in protostellar sources with a wide range of masses

(e.g., Anglada et al. 2018; Tychoniec et al. 2018). We will discuss these SEDs in detail in Section 5.

4. HRLs

$\text{H}3\alpha$ HRL emission is detected toward sources 2 and 3. Figure 6 shows the integrated $\text{H}3\alpha$ emission maps of these two sources and their $\text{H}3\alpha$ spectra at the continuum peak positions. The $\text{H}3\alpha$ peaks coincide well with the continuum peaks, which supports the existence of small ionized regions at the centers of sources 2 and 3 that contribute both to the $\text{H}3\alpha$ emission and the free-free continuum emission. Even though the $\text{H}3\alpha$ emission in source 2 is only detected with low signal-to-noise ratio (S/N) (6σ), the fact that the broad spectral feature is spatially coincident with the continuum emission suggests that the $\text{H}3\alpha$ detection is likely real. The $\text{H}3\alpha$ lines are relatively well fitted with Gaussian profiles. The $\text{H}3\alpha$ central velocities are derived to be $29.4 \pm 2.2 \text{ km s}^{-1}$ and $30.2 \pm 0.2 \text{ km s}^{-1}$ for sources 2 and 3, respectively, which are similar to each other within the uncertainties, and also consistent with the systemic velocity of source 2 ($30.0 \pm 0.3 \text{ km s}^{-1}$) estimated by fitting the Keplerian disk kinematics traced in different molecular lines (Sánchez-Monge et al. 2013). The line widths are derived to be $86.1 \pm 5.2 \text{ km s}^{-1}$ and $45.0 \pm 0.6 \text{ km s}^{-1}$ for sources 2 and 3, respectively. The line width of 86 km s^{-1} is on the upper edge of observed recombination line widths in hypercompact H II (HCH II) regions (e.g., Hoare et al. 2007). Although, larger line widths have been reported in some HCH II regions (e.g., NGC 7538 IRS 1; Sewilo et al. 2004); a line width of $\lesssim 50 \text{ km s}^{-1}$ is more typical for such regions.

Panels (e) and (f) of Figure 6 show the velocity structures of the $\text{H}3\alpha$ lines in sources 2 and 3. The integrated maps of the blue- and redshifted emission show a shift of emission with velocity in these two sources. For source 3, the high S/N further allows us to determine the shift of the emission centroid with channel velocity (Figure 7). The centroid positions are determined by fitting Gaussian ellipses to the $\text{H}3\alpha$ emission in the C3+C6+C9 configurations at channels with peak intensities $>10\sigma$. Following the method used by Zhang et al. (2019c), the uncertainties of the centroid positions are determined from the data S/N as well as the phase noise in the passband calibrator. The centroid distributions and kinematics are consistent with a rotating structure with a radius of about 5 mas (11 au). The elliptical distribution of the centroids, and the fact that the centroids with the highest velocities are closer to the center, are similar to what has been seen in molecular lines around massive protostars (e.g., Sánchez-Monge et al. 2013; Ilee et al. 2016), which indicates faster rotation velocities near the central source, as expected for a Keplerian disk.

Following the methods used by Sánchez-Monge et al. (2013) and Ilee et al. (2016), we fitted the $\text{H}3\alpha$ centroid distribution with a model of a Keplerian disk. The model has six free parameters: mass of the central object, the R.A. and decl. offsets of the center, disk position angle, disk inclination, and systemic velocity. The fitting minimizes the differences between the channel velocity and the line-of-sight velocity of disk rotation at the peak position of each channel. However, in our case, different combinations of disk inclination and central mass can generate fitting with similarly good qualities. Therefore, we cannot well constrain these two properties solely by such fittings. To break the degeneracy, we set the central mass to $16M_{\odot}$, which is estimated from the free-free continuum (see

Table 2
Identified Compact Continuum Sources in ALMA 1.3 mm Observations

Source	VLA Source ^a	Associated Core ^b	α (ICRS) hh:mm:ss	δ (ICRS) ° ' "	$I_{\text{peak},1.3 \text{ mm}}^{\text{c,d}}$ (mJy beam ⁻¹)	$S_{1.3 \text{ mm}}^{\text{c,e}}$ (mJy)	Mass ^g (M_{\odot})	Radius ^h (au)	Driving Outflow ⁱ
1	3	A	18:58:12.953	1:40:37.359	22.99 ± 0.06	42.19 ± 0.15 (42) ^f	0.70	35	Outflow 2
2	8a	B	18:58:13.037	1:40:35.931	27.80 ± 0.06	35.20 ± 0.15 (25) ^f	0.42	17	Outflow 1
3	1		18:58:12.815	1:40:36.604	13.03 ± 0.06	14.52 ± 0.16 (9.7) ^f	0.16	<12	
4	8b	B	18:58:13.015	1:40:36.110	1.37 ± 0.06	1.49 ± 0.15 (1.3) ^f	0.021	<36	
5			18:58:12.991	1:40:36.200	0.74 ± 0.06	1.05 ± 0.15	0.067	<39	
6			18:58:12.992	1:40:36.338	0.75 ± 0.06	0.95 ± 0.15	0.060	17	
7			18:58:13.070	1:40:35.768	1.07 ± 0.06	1.29 ± 0.15	0.083	15	
8			18:58:13.111	1:40:35.831	0.65 ± 0.06	0.65 ± 0.15	0.040	<39	
9			18:58:13.070	1:40:37.597	1.89 ± 0.06	3.65 ± 0.15	0.23	34	
10			18:58:12.921	1:40:39.988	0.86 ± 0.06	1.57 ± 0.16	0.10	33	
11		D	18:58:12.815	1:40:40.000	0.89 ± 0.07	3.77 ± 0.17	0.24	257	
12			18:58:12.836	1:40:34.715	1.21 ± 0.06	2.42 ± 0.16	0.15	37	
13			18:58:12.725	1:40:35.606	0.58 ± 0.07	0.74 ± 0.17	0.047	11	
14		C	18:58:13.131	1:40:33.233	2.98 ± 0.06	6.60 ± 0.16	0.42	44	Outflow 3
15			18:58:13.301	1:40:34.313	0.74 ± 0.07	1.88 ± 0.17	0.12	52	
16			18:58:12.957	1:40:30.656	2.12 ± 0.07	4.57 ± 0.17	0.29	38	
17		E	18:58:13.190	1:40:30.678	0.99 ± 0.07	0.99 ± 0.18	0.043	<30	Outflow 4
18			18:58:12.883	1:40:31.778	1.00 ± 0.07	1.48 ± 0.17	0.094	27	
19			18:58:12.858	1:40:26.403	0.77 ± 0.09	1.51 ± 0.23	0.096	34	
20			18:58:12.290	1:40:36.928	0.80 ± 0.10	1.55 ± 0.25	0.099	32	
21			18:58:13.955	1:40:27.608	1.64 ± 0.20	3.14 ± 0.48	0.20	44	
22			18:58:12.002	1:40:46.487	3.05 ± 0.30	7.83 ± 0.74	0.50	57	

Notes.

^a Compact sources identified from VLA observations by Beltrán et al. (2016).

^b Core structures identified from ALMA 0.85 mm observations by Sánchez-Monge et al. (2014). A source is considered to be associated with one of the identified cores only if it is close to the continuum peak of that core.

^c Primary beam response has been corrected for the peak intensities, integrated flux densities and their uncertainties.

^d Peak intensity measured from the C9 configuration image.

^e Flux density integrated over a circle with a radius of $0''.05$. The flux density uncertainties are estimated by calculating flux densities with apertures of the same size ($0''.05$) over random off-source positions many times on the primary beam uncorrected map, and then scaled by the primary beam response at that source position.

^f Numbers in the bracket show the dust continuum flux densities, after subtraction of the free-free emission. The free-free flux densities are estimated from the model fitting to the continuum SED and H30 α flux.

^g Gas mass calculated from dust continuum flux densities. A gas-to-dust mass ratio of 100 is assumed. For sources 1–4 (massive sources with photoionized regions), a dust temperature of 100 K is assumed, and for sources 5–22, a dust temperature of 30 K is assumed.

^h Defined as $\sqrt{D_{\text{maj}}D_{\text{min}}}/2$, where D_{maj} and D_{min} are the major axes FWHM and minor axis FWHM of the Gaussian component of the continuum image after deconvolution of the synthesized beam. The 2D Gaussian fit is performed using the CASA task *imfit*. Upper limits are given if the source is unresolved.

ⁱ Identified from ¹²CO maps (see Section 6.2).

Section 5.2). Figure 7(b) shows the best-fit model. This model has a systemic velocity of $V_{\text{sys}} = +30 \text{ km s}^{-1}$, R.A. offset of $\Delta\alpha = 1.2 \text{ mas}$, decl. offset of $\Delta\delta = 0.2 \text{ mas}$, position angle of the disk major axis of P.A. = 28° , and disk inclination of $i = 26^\circ$ between the disk plane and plane of sky. Although such a simple model fitting cannot rule out other possibilities for the observed H30 α kinematic pattern, it shows that disk rotation around a forming massive star can be a valid explanation.

While the velocity gradient of the ionized gas in source 3 could trace a rotating disk, it is more difficult to tell whether the velocity gradient seen in source 2 (Figure 6(e)) is real or not, or what its possible origin is if it is real, due to the low S/N. The direction of the tentative H30 α velocity gradient in source 2 is at a position angle of P.A. $\approx 25^\circ$. The disk around source 2 has a position angle of P.A. $\approx -25^\circ$ (see Section 6; also Sánchez-Monge et al. 2013), and the ionized jet originating from source 2 has a position angle of P.A. $\approx 20^\circ$ close to the source, as the jet has an S-shape morphology (Beltrán et al. 2016). Therefore the direction of the velocity gradient of the H30 α line is consistent with the jet direction. However, the line-of-sight velocity directions seen in the H30 α line (redshifted in the north and blueshifted in the south) are opposite of the outflows.

Molecular line observations have shown that the blueshifted molecular outflow is toward the north and NE, while the redshifted outflow is toward the south and southwest (Gibb et al. 2003; Birks et al. 2006; Qiu et al. 2013; see Section 6.2). The atomic line observations show that the jet toward the north is blueshifted (Fedriani et al. 2019). The jet-associated H₂O masers have also been reported to be redshifted ($V_{\text{lsr}} > 30 \text{ km s}^{-1}$) toward the south. Therefore, despite the fact that the velocity gradient orientation is similar to the jet direction, it is difficult to confirm that the velocity gradient is mainly tracing outflow motion. One possibility is that the observed H30 α velocity gradient is affected by the disk's rotation (redshifted on the northern side). In fact, in this source, the Br γ , an NIR HRL, does show one high-velocity component associated with the jet and a slow component associated with the disk (Fedriani et al. 2019), supporting that the ionized gas in this source is in both outflow and disk. Another possibility is that the jet is close to edge-on and therefore the inclination of the innermost part of the outflow is different from that of the outflows at larger distances.

As there are more and more 100-au-scale observations toward massive star-forming regions, kinematics of photo-ionized gas at disk scales around forming massive stars traced

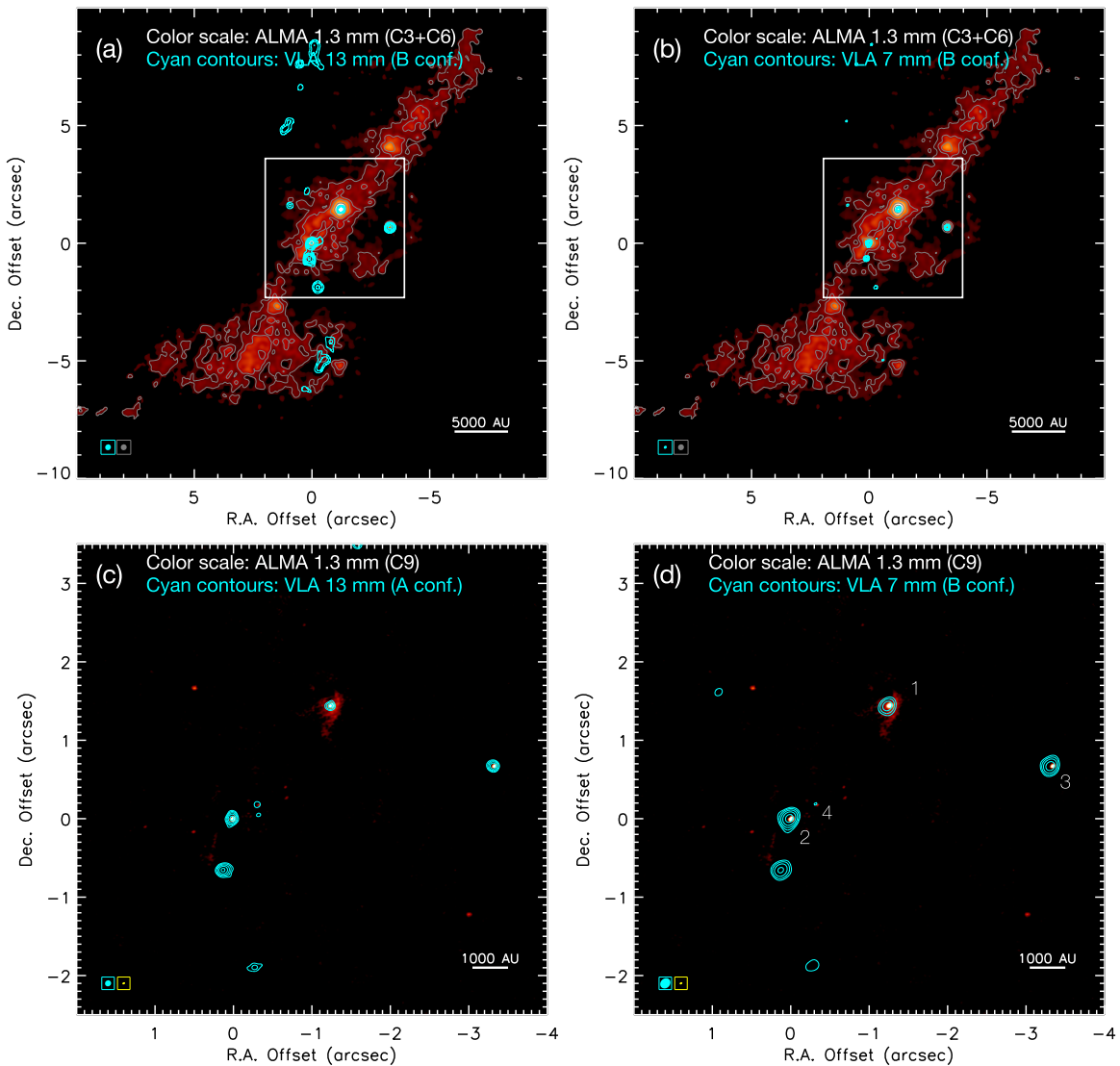


Figure 4. ALMA 1.3 mm continuum images (color scale) overlaid with VLA 1.3 cm (left column) and 7 mm (right column) continuum images (cyan contours). The wavelengths and configurations of the images are labeled in each panel. Panels (c) and (d) show zoom-in views of the central region (the white squares in panels (a) and (b)). The synthesized beams of the images are listed in Table 1. The contours start from 5σ and have intervals of 10σ . The 1σ rms noise levels of each image are listed in Table 1. The compact continuum sources identified in ALMA 1.3 mm images with corresponding VLA emissions are labeled in panel (d).

by recombination lines have started to be reported. This includes ionized disks (some are surrounded by neutral disks traced by molecular lines) and ionized outflows just launched from the disk (some are corotating with the disk) (e.g., Zhang et al. 2017; Zhang et al. 2019b, 2019c; Guzman et al. 2020; Jiménez-Serra et al. 2020; Moscadelli et al. 2021). These observations show the effectiveness of using recombination lines as a tracer of the ionized gas in the innermost region around forming massive stars to study accretion and photo-ionization feedback processes in massive star formation.

5. Fitting the Continuum and H30 α Fluxes

For sources 1–4, Figure 5 shows that most SEDs in the VLA bands have spectral indices between 0 and 2, indicating partially optically thick free–free emission. The optical depth of the free–free emission is dependent on the frequency (see the Appendix). For an ionized region with a uniform electron density, a spectral index of $\alpha \approx 1$ is only seen in a relatively narrow transition frequency range. However, in our detected

sources, the intermediate spectral indices are seen over a wide range of frequencies, which requires a density gradient in the ionized gas (e.g., Keto 2003).

We construct a simple model to explain the observed free–free continuum. The total H30 α fluxes are also used to constrain the model. The model details are introduced in the Appendix. In the model, we assume the emitting region is a circular disk on the plane of sky, and the emission measure ($EM = \int n_e^2 dl$) follows a power-law dependence on the radius ($EM \propto r^{\rho_{EM}}$). The three free parameters of the model are the electron temperature of the ionized gas (T_e), the emission measure at the radius of 10 au (EM_{10au}), and the power-law index of the emission measure distribution ρ_{EM} . The fitting results are listed in Table 3. Below we discuss the fitting results of each source in detail.

5.1. ALMA Source 2

For source 2, we simultaneously fit the VLA continuum fluxes (assuming they are free–free dominated) and H30 α flux.

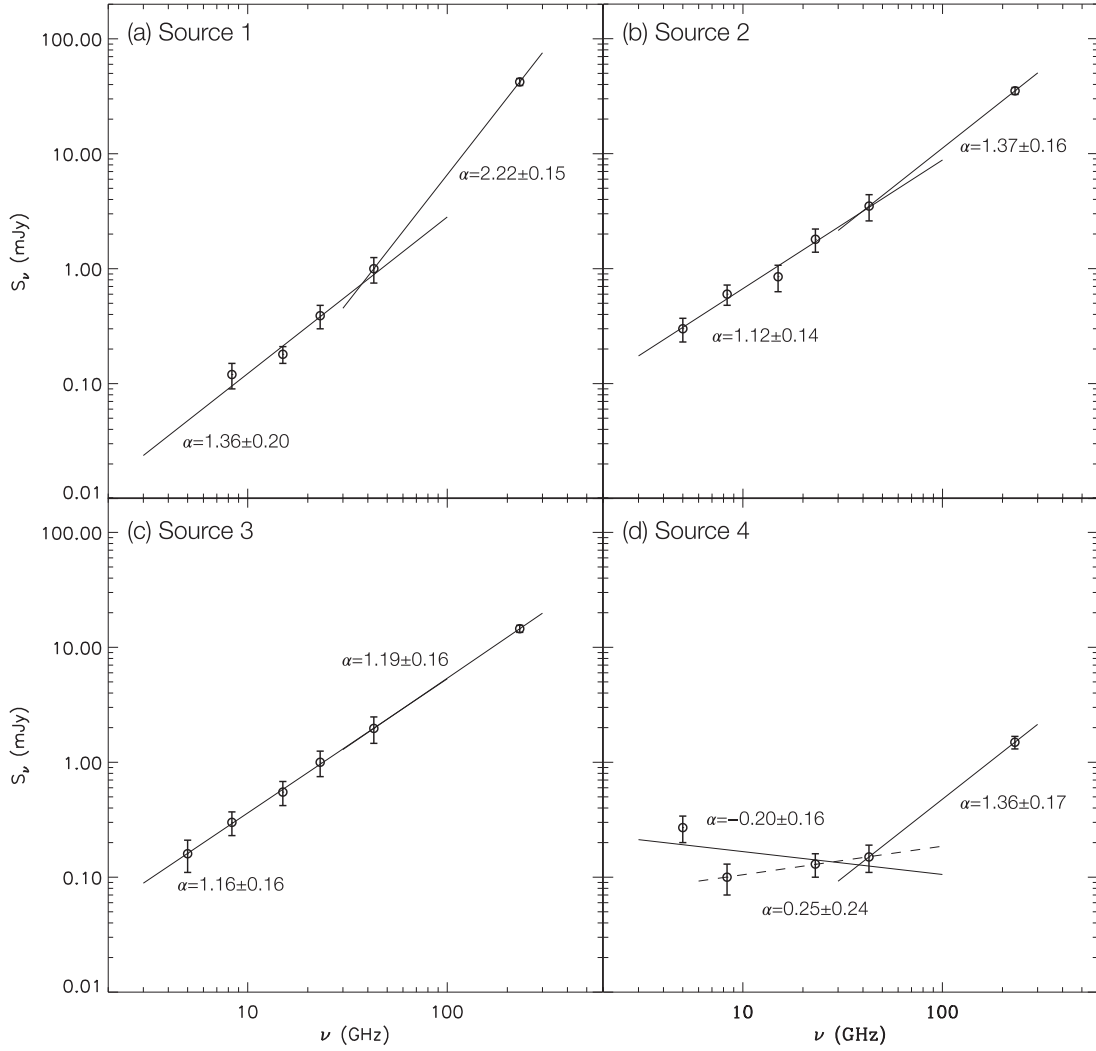


Figure 5. SEDs (symbols and error bars) comprising VLA and ALMA 1.3 mm continuum flux densities, for the 1.3 mm compact sources with VLA detections, i.e., ALMA sources 1–4. The ALMA 1.3 mm flux densities are measured from the C9 configuration image and are listed in Table 2. The VLA flux densities are taken from Beltrán et al. (2016). An additional 7% of uncertainties due to absolute flux calibration are added to the ALMA 1.3 mm flux densities. The power-law fit to the VLA fluxes, and between VLA 7 mm and ALMA 1.3 mm, are shown by the solid lines. In source 4 (panel (d)), the dashed line shows the power-law fit to the VLA fluxes excluding the 6 cm flux.

Table 3
Parameters of the Best-fit Models of Continuum SED and H30 α Flux

Source	T_e (10^4 K)	$EM_{10\text{au}}$ (10^9 pc cm $^{-6}$)	ρ_{EM}	$n_{e,10\text{au}}$ (10^7 cm $^{-3}$)	α_{dust}	\dot{N}_i^a (10^{46} s $^{-1}$)	$m_{*,ZAMS}$ (M_\odot)	Spectral Type	$L_{*,ZAMS}$ ($10^3 L_\odot$)
Source 1	1.0	0.2	2	0.2	2.3	0.009–1	7.3–12.0	B2–B0.5	1.8–9.0
Source 2	0.9	20	3	2		0.8–48	11.7–18.4	B0.5–O9.5	8.4–31
Source 3	0.6	6.3	3	1.1		0.3–30	10.7–17.3	B1–B0	6.2–26
Source 4	1.2	0.2	2	0.2		0.013	7.6	B2	2.1

Note.

^a As \dot{N}_i is sensitive to ρ_{EM} , we show a range of \dot{N}_i if ρ_{EM} is not well constrained by the fitting (see text for details).

Figure 8 shows the best-fit model and the χ^2 distribution in the parameter space. The 1.3 mm continuum flux is not used in the fitting as it contains significant dust contribution. The ionized gas temperature and emission measure are both well constrained by the fitting, with the best-fit model having $T_e = 9000$ K and $EM_{10\text{au}} = 2 \times 10^{10}$ pc cm $^{-6}$. The power-law index of the emission measure gradient is not well constrained. The best-fit model has $\rho_{EM} = 3$, but all ρ_{EM} values between 2

and 3 can produce similarly good fits. Note that $\rho_{EM} = 2$ corresponds to a power-law index of $\rho_{n_e} = 1.5$ for the electron density gradient, which is consistent with a photoionized disk, while $\rho_{EM} = 3$ corresponds to a power-law index of $\rho_{n_e} = 2$ in the electron density gradient, which is consistent with an expansion flow (see the Appendix). The best-fit model with $\rho_{EM} = 3$ is therefore consistent with the wide recombination line (see Section 4). The derived $EM_{10\text{au}} = 2 \times 10^{10}$ pc cm $^{-6}$

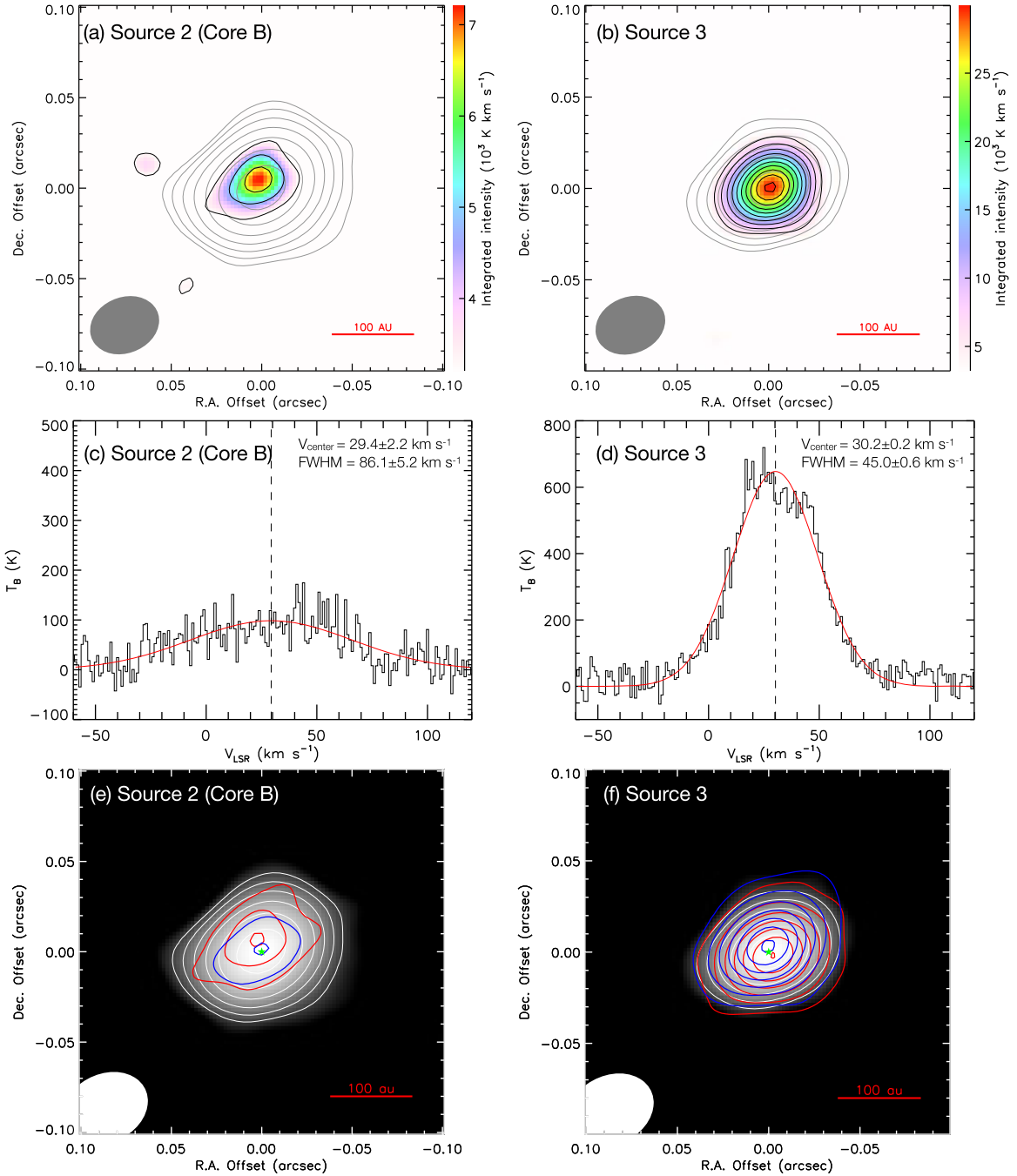


Figure 6. (a) Integrated emission map of the H30 α recombination line shown in color scale and black contours, overlaid with the continuum emission (gray contours), for ALMA source 2 (i.e., core B). Both line and continuum images are from the C9 configuration data. The H30 α emission is integrated into the range of $-5 \text{ km s}^{-1} < V_{\text{LSR}} < 70 \text{ km s}^{-1}$. The H30 α contours (black) start at 3σ and have intervals of 1.5σ , with $1\sigma = 0.045 \text{ Jy beam}^{-1} \text{ km s}^{-1}$ ($5.5 \times 10^2 \text{ K}$). The continuum contours (gray) in both panels have levels of $5\sigma \times 2^n$ ($n = 0, 1, \dots$), with $1\sigma = 0.061 \text{ mJy beam}^{-1}$ (1.4 K). (b) Same as panel (a), but for ALMA source 3, and the H30 α contours start at 5σ and have intervals of 5σ . (c) H30 α spectrum at the continuum peak position of ALMA source 2 (black curve), with a Gaussian fit shown by the red curve. The central velocity (shown by the vertical dashed line) and FWHM of the Gaussian fit are labeled. (d) Same as panel (c), but at the continuum peak position of ALMA source 3. (e) Integrated blueshifted and redshifted H30 α emission maps (blue and red contours) overlaid on the 1.3 mm continuum emission (grayscale and white contours) of source 2. The blueshifted and redshifted emission is integrated into the velocity ranges of $-5 \text{ km s}^{-1} < V_{\text{LSR}} < +30 \text{ km s}^{-1}$ and $+30 \text{ km s}^{-1} < V_{\text{LSR}} < +65 \text{ km s}^{-1}$, respectively. The blue and red contours have the lowest contour levels of 5σ and intervals of 2.5σ , where $1\sigma = 270 \text{ K km s}^{-1}$. The stars mark the continuum peak position. (f) Same as panel (a), but for source 3, and the blue and red contour intervals are 5σ .

also leads to an electron density of $n_e \simeq 2.0 \times 10^7 (l/10\text{au})^{-1/2} \text{ cm}^{-3}$ at 10 au scale (l is the line-of-sight scale of the ionized region). The compact size ($<100 \text{ au}$, seen from the image) of the ionized region, the derived emission measure and electron density, as well as the H30 α line width of 80 km s^{-1} , are all consistent with a HCH II region (e.g., Hoare et al. 2007).

From the fitted parameters T_e , $\text{EM}_{10\text{au}}$, and ρ_{EM} , we further estimate the ionizing photon rate \dot{N}_i (see the Appendix). Since \dot{N}_i is sensitive to ρ_{EM} (see the last term in Equation (A19)) and ρ_{EM} is not well constrained, the models with similarly good fit give a range of $\dot{N}_i = (0.8 - 48) \times 10^{46} \text{ s}^{-1}$, with $\dot{N}_i = 48 \times 10^{46} \text{ s}^{-1}$ being the best model (Figure 8(e)). For

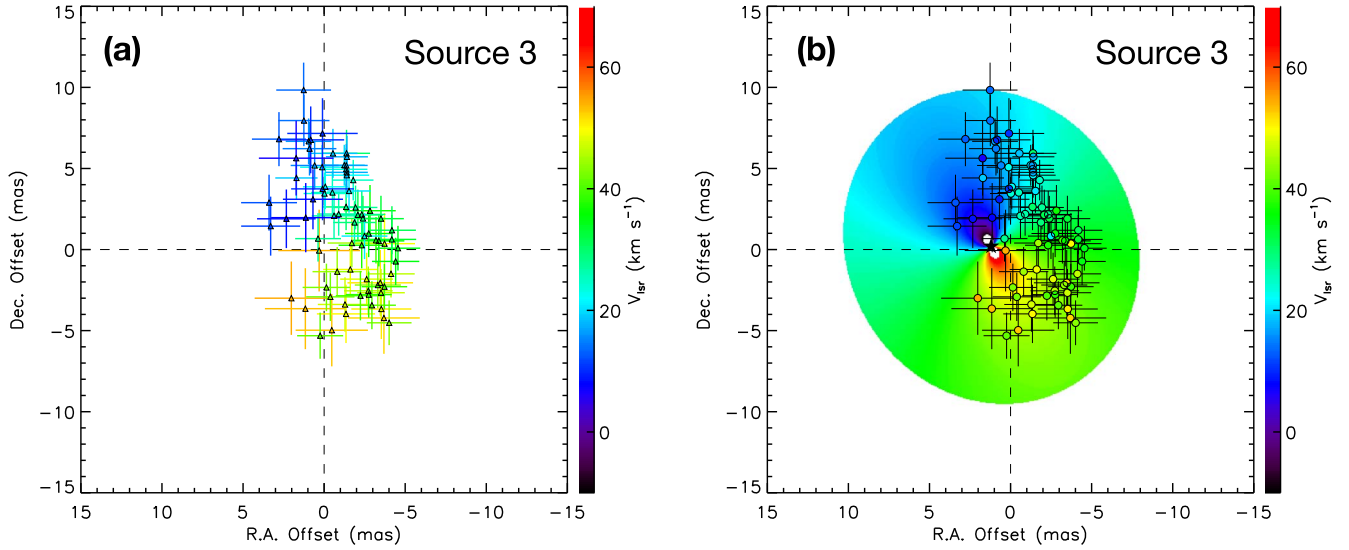


Figure 7. (a) Distribution of the H30 α emission centroids (triangles with error bars) in source 3. Only channels with peak intensities $>10\sigma$ ($1\sigma = 1.8 \text{ mJy beam}^{-1}$) are included. The position offsets are relative to the continuum peak. The line-of-sight velocities are shown by the color scale. (b) The best-fit disk model for the H30 α centroid distribution in source 3 (see the text for more details).

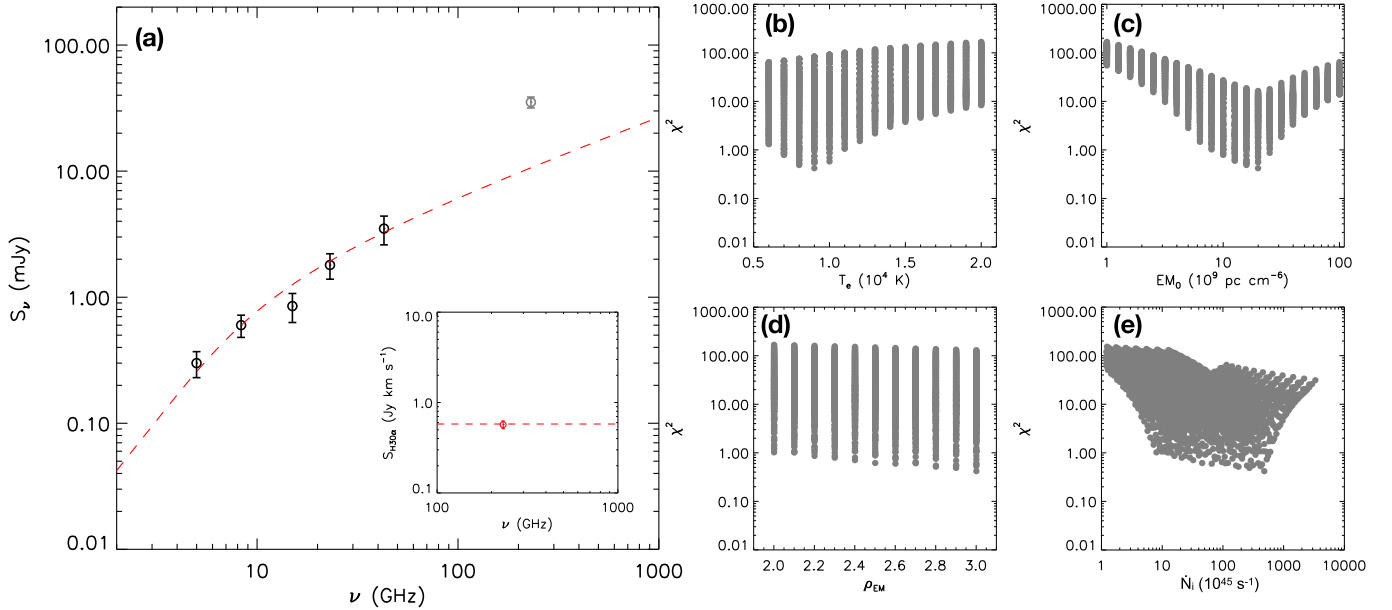


Figure 8. (a) The continuum SED of source 2 for the VLA bands and ALMA 1.3 mm continuum (data points). The red dashed line shows the free–free emission of the best-fit model. ALMA 1.3 mm continuum (shown in gray) is not used in the fitting. The inset panel shows the H30 α flux integrated over velocity and area (red data point) and the model fit (red dashed line). The model fits the continuum and H30 α fluxes simultaneously. (b)–(d) χ^2 distribution with model parameters: electron temperature T_e (panel (b)), the emission measure EM_0 at the radius of 10 au (panel (c)), and the power-law index of the emission measure distribution ρ_{EM} (panel (d)). (e) χ^2 distribution with the ionizing photon rate \dot{N}_i calculated from T_e , EM_0 , and ρ_{EM} .

zero-age main sequence (ZAMS) stars, this corresponds to a stellar mass of 11.7–18.4 M_\odot (Davies et al. 2011), i.e., the spectral type B0.5–O9.5 (Mottram et al. 2011). Our estimates of the emission measure, ionizing photon rate, and stellar mass, are higher than that estimated by Beltrán et al. (2016) ($EM = 2.7 \times 10^8 \text{ pc cm}^{-6}$, $\dot{N}_i = 1 \times 10^{45} \text{ s}^{-1}$, and B1-type ZAMS star). This is because their estimation is based on the assumption of optically thin free–free emission, and a uniform density distribution. In our model, we consider a gradient in the emission measure (and therefore the optical depth of free–free emission), which leads to higher values of ionizing photon rate and stellar mass. We note that the derived ZAMS mass should be treated as a reference mass because a forming massive star

that is still in a bloated phase before reaching the main sequence requires more mass than a ZAMS star to produce the same amount of ionizing photons (e.g., Hosokawa et al. 2010). Detailed protostellar evolution calculations taking into account various accretion histories of massive star formation show that accreting massive young stars with a wide range of mass have similar levels of ionizing photon rates (e.g., Zhang et al. 2014; Tanaka et al. 2016; Zhang & Tan 2018), which we will discuss in more details in Section 5.5.

The best-fit model gives a free–free flux of 10 mJy at 1.3 mm, leaving about 25 mJy to be the dust emission at 1.3 mm. Such a 1.3 mm dust emission flux leads to about 0.9 mJy of dust emission at 7 mm assuming an optically thick

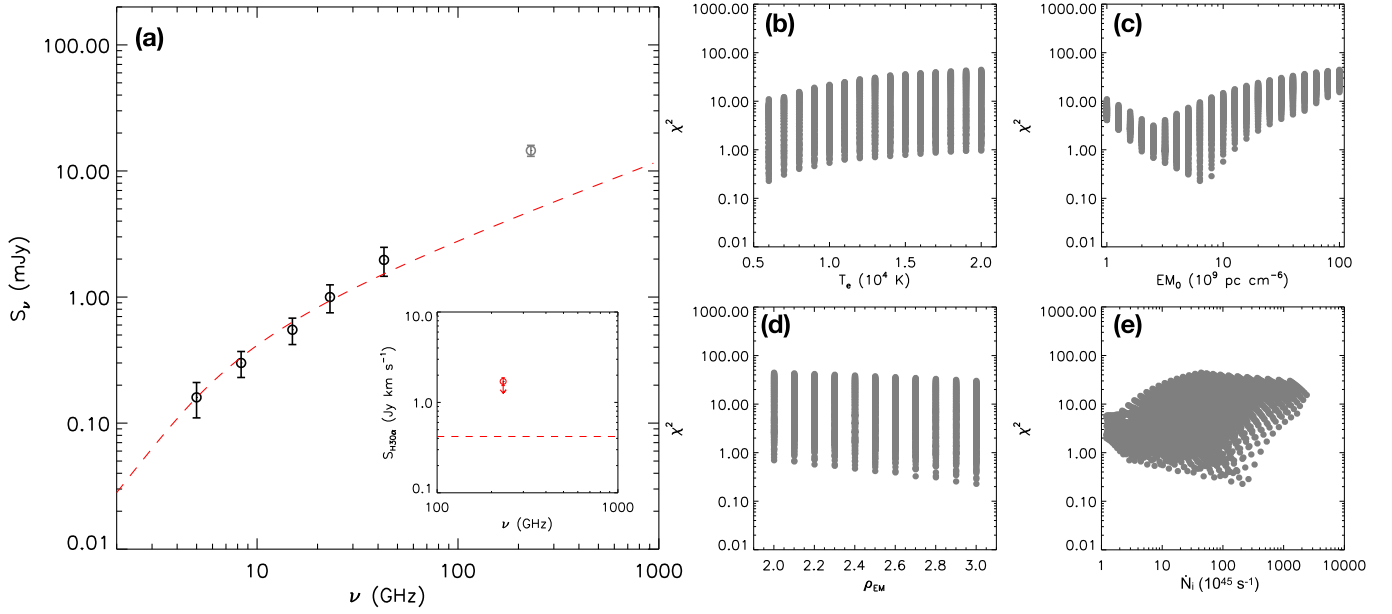


Figure 9. Same as Figure 8, but for ALMA source 3. As the H30 α line in this source has a potential maser component, we use it as an upper limit to constrain the model (inset of panel (a)).

dust spectral index of 2. The dust component will be much lower if an optically thin dust spectral index of 3 is used. This confirms that the continuum at 7 mm (and at lower frequencies) is indeed dominated by the free–free emission, and that the method of using a free–free continuum model to fit the VLA band continuum is valid.

5.2. ALMA Source 3

As shown in Section 4, source 3 has strong H30 α emission. The H30 α flux integrated over area and velocity is 1.7 Jy km s $^{-1}$. Under the local thermal equilibrium (LTE) condition, such an H30 α flux gives an optically thin limit of 1.3 mm free–free continuum ranging from 13 mJy with $T_e = 6000$ K to 51 mJy for $T_e = 20,000$ K (Equation (A11)). Such a free–free flux is higher than the observed total continuum flux at 1.3 mm, except for the low end of T_e . If the continuum is not optically thin, the intensity ratio between the recombination line (after subtracting the continuum) and the free–free continuum becomes even lower than that estimated in Equation (A11), which leads to an even higher free–free continuum flux. Therefore, the LTE condition for the H30 α of this source may be in question, i.e., the observed bright HRL emission in this source might be enhanced by maser emission. To date, millimeter HRL masers have been reported in a modest number of sources (MWC349A, Martín-Pintado et al. 1989; Jiménez-Serra et al. 2013; MonR2-IRS2, Jiménez-Serra et al. 2013; and G45.47+0.05, Zhang et al. 2019c). Here, we consider this to be another case of a possible millimeter HRL maser.

As we do not have a non-LTE effect in our simple model, we use the observed H30 α flux as an upper limit to constrain the model. Figure 9 shows the best-fit model and the χ^2 distribution in the parameter space. As neither the 1.3 mm continuum flux nor the H30 α flux is used in fitting, we cannot constrain well the free–free emission at millimeter wavelengths. The emission measure is relatively well constrained to $EM = 6.3 \times 10^9$ pc cm $^{-6}$ by the fitting, which leads to an electron density of $n_e \simeq 1.1 \times 10^7 (l/10\text{au})^{-1/2} \text{cm}^{-3}$ at the

10 au scale. The compact size, the derived emission measure and electron density, as well as the H30 α line width of 40 km s $^{-1}$ are also consistent with a HCH II region. The best-fit model has $T_e = 6000$ K and $\rho_{EM} = 3$, but the dependence of χ^2 on T_e and ρ_{EM} are relatively weak. As Figure 9(e) shows, the models with similarly good fit give a range of $\dot{N}_i = (0.3 - 30) \times 10^{46}$ s $^{-1}$, which corresponds to a ZAMS stellar mass of 10.7–17.3 M_\odot (Davies et al. 2011), i.e., the spectral type B1–B0 (Mottram et al. 2011). The best model has $\dot{N}_i = 2 \times 10^{47}$ s $^{-1}$, corresponding to a ZAMS stellar mass of 16.4 M_\odot .

5.3. ALMA Source 1

No H30 α emission is detected in the ALMA source 1 (core A or VLA source 2). The noise level of the integrated H30 α emission map is 0.06 Jy beam $^{-1}$ km s $^{-1}$. We use the 3σ level (0.18 Jy km s $^{-1}$) as the upper limit for the H30 α flux for this source. However, our free–free continuum and H30 α model failed to reproduce the VLA band continuum fluxes and the H30 α upper limit. The fact that the H30 α emission is weak and the spectral index between 1.3 and 7 mm is greater than 2 (see Figure 5), indicates that the dust emission may be significant even at 7 mm. Therefore, we include an additional dust component in the SED fitting (Equation (A16)). We assume that the ALMA 1.3 mm continuum is dominated by dust emission and use the dust spectral index α_{dust} as an additional free parameter. The best-fit model and the χ^2 distribution in the parameter space are shown in Figure 10. Note that since we only have five data points and one upper limit to constrain four free parameters, the constraints are relatively weak.

The emission measure and the dust spectral index are relatively well constrained. The best-fit model has $EM_{10\text{au}} = 2 \times 10^8$ pc cm $^{-6}$ (corresponding to an electron density of $n_e \simeq 2.0 \times 10^6 (l/10\text{au})^{-1/2} \text{cm}^{-3}$) and $\alpha_{\text{dust}} = 2.3$. On the other hand, the electron temperature T_e and the emission measure gradient power-law index ρ_{EM} are not constrained. The models with similarly good fit give an ionizing photon rate range of $\dot{N}_i = (0.09 - 10) \times 10^{45}$ s $^{-1}$, which corresponds to a

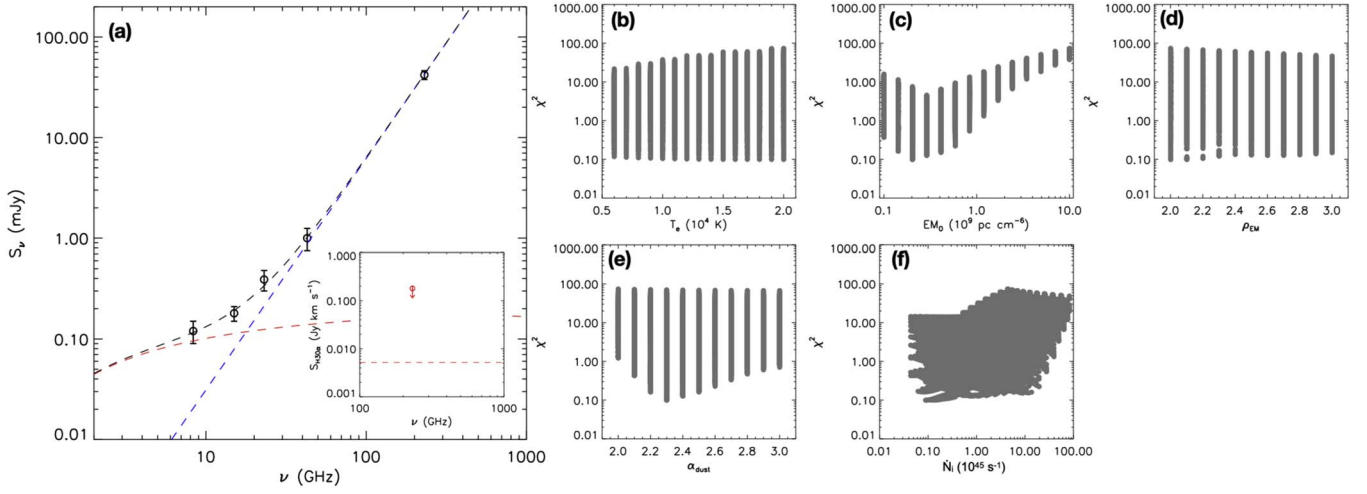


Figure 10. (a) The continuum SED of source 1 for VLA bands and ALMA 1.3 mm continuum (data points). The red dashed line shows the free–free emission of the best-fit model. The blue dashed line shows the dust emission of the best-fit model. The black dashed line shows the total continuum emission. The inset panel shows the 3σ level of the H30 α integrated map used as the upper limit (red data point) and the model prediction (red dashed line). (b)–(e) χ^2 distribution with model parameters: electron temperature T_e (panel (b)), the emission measure EM_0 at the radius of 10 au (panel (c)), the power-law index of the emission measure distribution ρ_{EM} (panel (d)), and the spectral index of the dust component α_{dust} (panel (e)). (f) χ^2 distribution with the ionizing photon rate \dot{N}_i calculated from T_e , EM_0 , and ρ_{EM} .

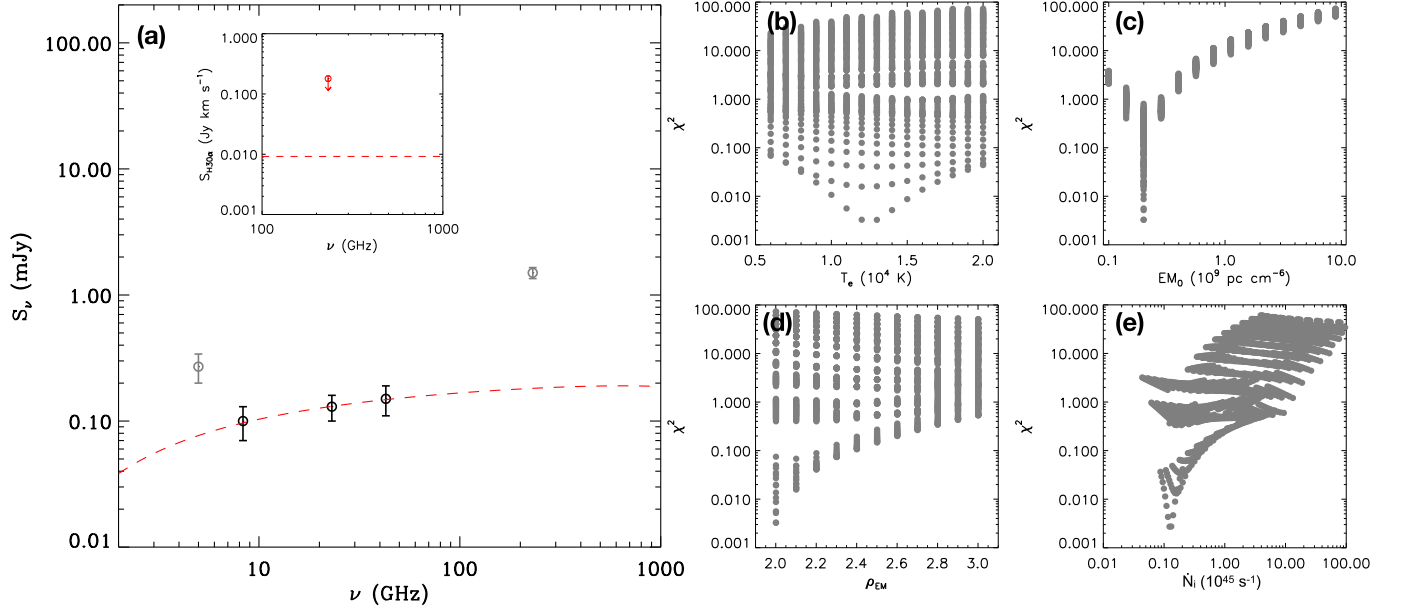


Figure 11. Same as Figure 8, but for ALMA source 4. The 6 cm flux is also not used in the fitting (see the text).

ZAMS stellar mass of 7.3–12.0 M_\odot and spectral type B2–B0.5. Interestingly, the derived emission measure and electron density are not very consistent with typical HCH II regions. However, the compact size seen at radio wavelengths, the low free–free continuum flux, and the derived low central stellar mass, suggest that this is an extremely young photoionization region.

5.4. ALMA Source 4

For source 4, the SED in the VLA frequency range is almost flat, indicating nearly optically thin free–free emission. Adopting the same method used for sources 2 and 3, we fit the three VLA bands with constraints for the upper limit of the H30 α integrated flux ($3\sigma = 0.18$ Jy km s $^{-1}$). The results are shown in Figure 11. Note that we do not include the 6 cm continuum in the fitting, as it is significantly higher than the

other VLA continuum fluxes (see Figure 5(d)), which may be caused by nonthermal emission, which has negative indices. The ALMA 1.3 mm continuum is also not used because it has a significant contribution from dust emission. The best-fit model has $T_e = 12,000$ K, $\text{EM}_{10\text{au}} = 2 \times 10^8$ pc cm $^{-6}$, and $\rho_{\text{EM}} = 2$. These parameters lead to an ionizing photon rate of $\dot{N}_i = 1.3 \times 10^{44}$ s $^{-1}$, which corresponds to a ZAMS stellar mass of 7.6 M_\odot and spectral type B2.

However, as discussed in Section 3.2, while source 4 could be a forming massive star creating a small ionized region via photoionization like the fitting model assumes, its low 1.3 mm continuum emission (on the same level as other low-mass sources in the region) suggests that it could also be a low-mass protostar with free–free emissions caused by shock-induced ionization from an unresolved jet. In fact, the negative spectral index in the low-frequency range could indicate the

Table 4
Parameters of the Observed Lines^a

Species	Transition	Frequency (GHz)	E_u/k (K)	$S\mu^2$ (D^2)	Velocity Resolution (km s ⁻¹)	Synthesized Beam	Channel rms (mJy beam ⁻¹)
H	30 α	231.90090			0.63	0''039 \times 0''031 (P. A. = - 68 $^\circ$ 0)	1.7
SO ₂	22 _{2,20} - 22 _{1,21}	216.6433035	248	35.3	0.68	0''30 \times 0''29 (P. A. = - 3 $^\circ$ 5) 0''052 \times 0''040 (P. A. = - 63 $^\circ$ 9)	3.3 1.9
CH ₃ OH	4 _{2,2} - 3 _{1,2} ; E	218.4400630	45.5	13.9	0.68	0''29 \times 0''28 (P. A. = - 5 $^\circ$ 9) 0''052 \times 0''040 (P. A. = - 64 $^\circ$ 3)	5.6 2.0
H ₂ CO	3 _{2,1} - 2 _{2,0}	218.7600660	68.1	9.06	0.67	0''29 \times 0''28 (P. A. = - 3 $^\circ$ 7)	5.4
H ₂ S	2 _{2,0} - 2 _{1,1}	216.7104365	84.0	2.06	0.68	0''30 \times 0''29 (P. A. = - 4 $^\circ$ 9)	3.4
SiO	5 - 4	217.1049190	31.3	48.0	0.67	0''30 \times 0''29 (P. A. = - 8 $^\circ$ 6)	2.9
CH ₃ OCH ₃	13 _{0,13} - 12 _{1,12} ; AA	231.9877830	69.8	170	0.63	0''28 \times 0''27 (P. A. = - 36 $^\circ$ 5)	2.9
	13 _{0,13} - 12 _{1,12} ; EE	231.9878580	69.8	272			
	13 _{0,13} - 12 _{1,12} ; AE	231.9879320	69.8	102			
	13 _{0,13} - 12 _{1,12} ; EA	231.9879330	69.8	68.0			
¹² CO	2 - 1	230.5380000	16.6	0.0242	0.63	0''28 \times 0''27 (P. A. = - 14 $^\circ$ 1)	4.0

Note.

^a Molecular line information taken from the CDMS database (Müller et al. 2005).

contribution of nonthermal emission caused by the jet shock. Another supporting evidence is that if the free-free emission is caused by photoionization, the mass ratio between sources 2 and 4 is 2–3 as estimated above. If sources 2 and 4 are indeed a binary system, the existence of such a massive companion should have a significant impact on the circumbinary disk structure. However, as we will show in Section 6.1, the disk structure is highly symmetric with respect to source 2 indicating little to no impact from source 4.

5.5. Consistency of Stellar Mass Estimation

In the above discussion, we estimate the stellar masses from the ionizing photon rates \dot{N}_i using the ZAMS stellar model, in which a value of \dot{N}_i corresponds to a single value of the stellar mass m_* . Here, we discuss the uncertainty of this method, comparing it to the dynamical masses and the constraints from infrared luminosity.

A dynamical mass of $18 M_\odot$ was derived by fitting the molecular line kinematics of the rotational structure around sources 2 and 4 (Sánchez-Monge et al. 2013). Using the ZAMS ionizing rate, we estimate a total mass of about 18 – $26 M_\odot$, which is close to, but slightly larger than, the dynamical mass of $18 M_\odot$. This difference can be completely due to uncertainties in both methods of mass estimation. The mass estimated from the ionizing rate can be lower if some fraction of the free-free emission in source 4 is not caused by photoionization, as discussed above. In that case, the total mass would be more consistent with the dynamical mass. For source 1, previous studies of molecular lines provided a dynamical mass of about $4 M_\odot$ assuming the emission is from a Keplerian disk (Sánchez-Monge et al. 2014). As shown in Section 6.1.3, we improve the estimation of dynamical mass to about $6 M_\odot$ as the source 1 disk is not rotationally supported. This new dynamical mass is close to the mass evaluated from the ZAMS ionizing rate (7.3 – $12 M_\odot$).

Next, we compare the infrared luminosity and the expected luminosity from the ionizing photon rate and the ZAMS model. As the sources are embedded in the opaque dusty cloud, infrared observations provide only the total luminosity rather than the individual ones. Under the assumption of the isotropic radiation, the total bolometric luminosity of the region is $L_{\text{bol,iso}} \approx 3 \times 10^4 L_\odot$, found by integrating the infrared SED

(e.g., Sánchez-Monge et al. 2014). More accurately, the SED fittings, which take into account the photon escape along the outflow cavity, gave the bolometric luminosity of $L_{\text{bol}} \approx (4$ – $22) \times 10^4 L_\odot$ (Zhang et al. 2013; De Buizer et al. 2017; Zhang & Tan 2018). Although a single protostar was assumed in these fittings, the obtained total luminosity is reasonable for the multiple-source system as the ratio between L_{bol} and $L_{\text{bol,iso}}$ mostly depends on the distribution of the surrounding material. On the other hand, Table 3 lists the expected luminosities from the ionizing photon rates and the ZAMS model for each source. Their total of $(1.8$ – $6.8) \times 10^4 L_\odot$ is within the consistent range of the bolometric luminosity L_{bol} from the model fittings, suggesting that our mass estimation from the ionizing rates is reasonable. We note again that, however, an accreting massive protostar tends to have a bloated cool photosphere emitting fewer ionizing photons than the ZAMS star with the same luminosity (Hosokawa & Omukai 2009; Hosokawa et al. 2010; Haemmerlé & Peters 2016; Tanaka et al. 2016). It could explain why the total expected luminosity from the ZAMS ionizing rate (Table 2) is possibly lower than L_{bol} .

In summary, the mass estimates from our free-free and H30 α model fits are generally consistent with other constraints from kinematics and infrared luminosity. A more accurate mass estimation should simultaneously take into account all the constraints discussed above, including ionizing photon rate, bolometric luminosity, and kinematics, using realistic massive protostellar evolution models rather than simple ZAMS stellar models.

6. Molecular Line Observations

Our observations include various molecular lines tracing different gas structures in the region. Here, we present results for the SO₂(22_{2,20} - 22_{1,21}), H₂CO(3_{2,1} - 2_{2,0}), CH₃OH(4_{2,2} - 3_{1,2}; E), H₂S(2_{2,0} - 2_{1,1}), and CH₃OCH₃(13_{0,13} - 12_{1,12}) lines, which trace dense gas, and ¹²CO(2-1) and SiO(5-4), which trace outflows. The observing parameters for these lines are listed in Table 4. These lines are the main targeted lines of our spectral window setups. While some other weaker lines are also detected in the same spectral windows, we defer the analysis of the full molecular line data to a future study.

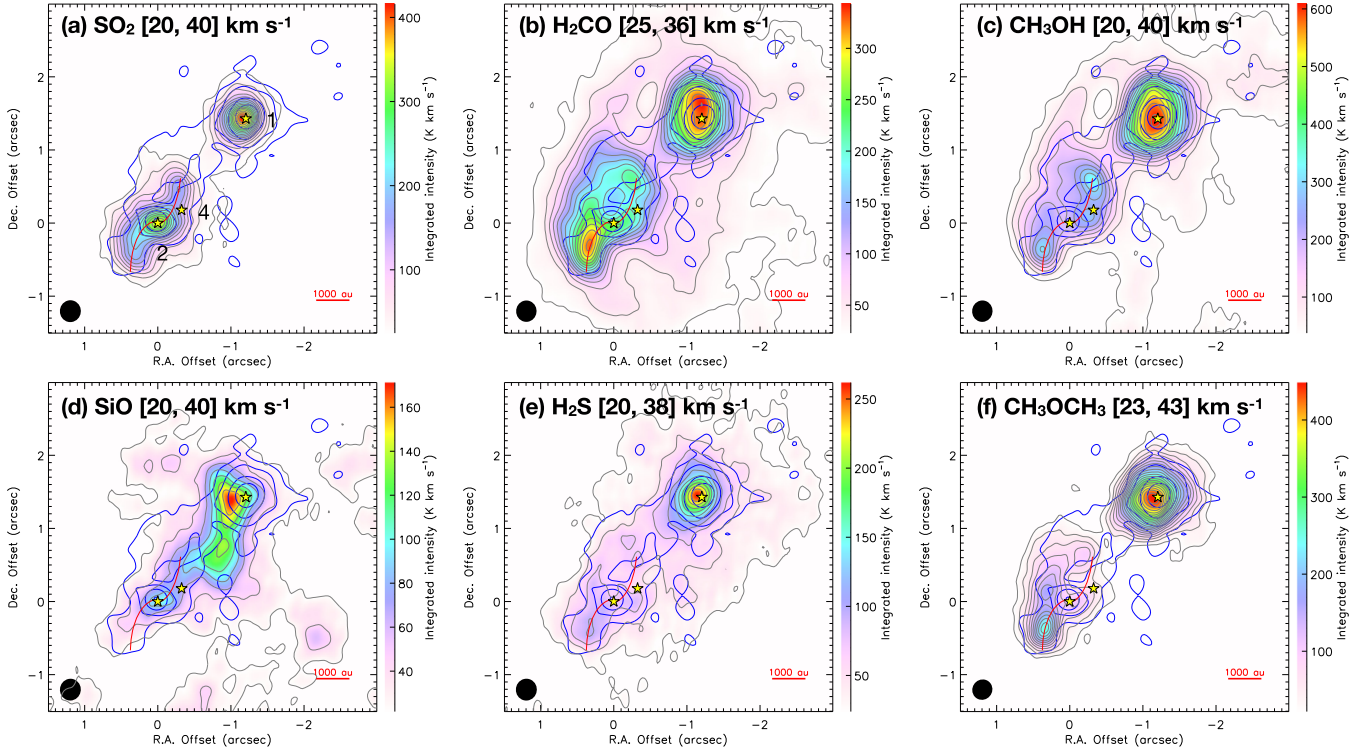


Figure 12. Integrated intensity maps of different emission lines (color scale and gray contours) overlaid with the 1.3 mm continuum emission (blue contours). The molecule names and integrated V_{LSR} ranges are labeled in each panel. The continuum contour levels are at $10\sigma \times 2^n$ ($1\sigma = 0.48 \text{ mJy beam}^{-1}$, $n = 0, 1, \dots$). The line emission contours have the lowest level and intervals of 3σ , with $1\sigma = 8.3, 7.6, 12.5, 7.3, 8.0,$ and 7.2 K km s^{-1} in panels (a)–(f), respectively. The yellow stars mark the positions of sources 1, 2, and 4 identified from the C9 configuration data (source names are labeled in panel (a)). The red curve shows the spiral structure fitted from the SO_2 integrated map.

6.1. Multi-scale Accretion Structures

Figure 12 shows the integrated emission maps of the SO_2 , H_2CO , CH_3OH , SiO , H_2S , and CH_3OCH_3 lines. Here, we focus on the molecular lines associated with the central sources, especially source 1 (core A), and sources 2 and 4 (core B). For source 1, the line emission is mostly concentrated near the source center (except for the SiO emission whose peak is more offset). However, these lines show different spatial distributions around source 2. Note that sources 2 and 4 are proposed to form a binary system by Beltrán et al. (2016) based on their closeness and mass estimates. However, it is still unclear whether they are a true bound binary system, or how they relate to the nearby other sources identified in 1.3 mm long-baseline data.

The SO_2 emission around source 2 is concentrated toward the center, and shows a morphology consistent with that of two spiral structures that are symmetric with respect to the center (Figure 12(a)). In contrast to the SO_2 line, the center is devoid of H_2CO and CH_3OH emissions. While the spiral structures are still distinguishable in the H_2CO and CH_3OH emission, they mainly show an elliptical ring around sources 2 and 4. In addition, the H_2CO and CH_3OH lines further show a stream of emission to the north of source 2 that connects to source 1, forming a larger elliptical shape surrounding sources 1 and 2. The aspect ratio of this larger elliptical structure is about 2:1. If we assume that this structure is circular, then the inclination between its midplane and the line of sight is about 30° . This is close to the derived inclination of the disk around source 2 estimated from previous observations (Sánchez-Monge et al. 2013). Therefore, despite the fact that material is distributed in the filament-like structure on a larger scale, there may be a

near-circular structure with a radius of about 4000 au around the two main forming massive stars (sources 1 and 2), which then feeds into two separate disks feeding each source. In addition, the disk feeding source 2 (and source 4) has formed spiral structures.

The kinematics of these lines are consistent with such a scenario. Figures 13 and 14 show the channel maps of the SO_2 and CH_3OH lines around these sources. The spiral structures around source 2 seen in the integrated maps have highly symmetric and ordered velocity structures, with the southeastern arm blueshifted and the northwest (NW) arm redshifted. Source 1 (core A) is slightly more redshifted than source 2 (core B), and the stream connecting these two sources (Figure 14) is redshifted with respect to source 2 and joins the source 1 disk at a velocity slightly more redshifted than the source 1 systemic velocity.

Compared to the H_2CO and CH_3OH lines, the H_2S and CH_3OCH_3 emissions are more concentrated around the two main sources, but their morphologies are similar to the H_2CO and CH_3OH lines. SiO emission around source 2 appears to follow the spiral arm structures seen in the SO_2 line. However, SiO emission is widely spread out in this region with multiple components tracing outflows (originated from source 1) and emission along the filament, as we will discuss in more detail in Section 6.2. Therefore, it is difficult to conclude that the SiO emission around source 2 actually traces the disk spiral structure.

6.1.1. Velocity Structure around Source 2

Figure 15 shows the position–velocity (PV) diagrams along a position angle of $\text{P.A.} = -25^\circ$ across source 2 to show the

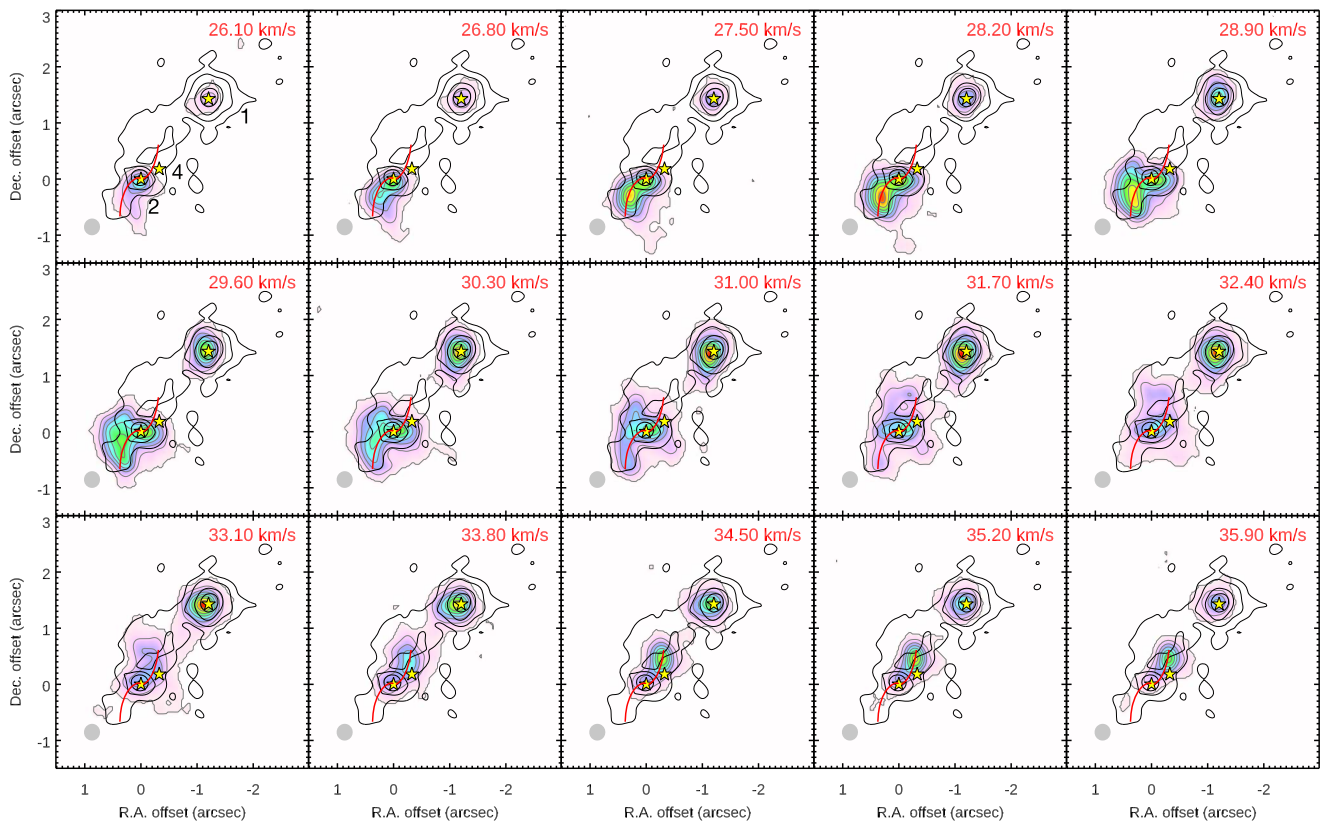


Figure 13. Channel maps of the SO₂ (22_{2,20} – 22_{1,21}) emission (color scale and gray contours). The central velocity of each channel is labeled in each panel. The gray contours start at 3 σ and have intervals of 6 σ (1 σ = 3.3 mJy beam⁻¹). The black contours show the continuum emission (same as Figure 12). The yellow stars mark the positions of sources 1, 2, and 4 identified from the C9 configuration data (source names are labeled in the top-left panel). The red curve shows the spiral structure fitted from the SO₂ integrated map. The synthesized beam is shown in the lower-left corner of each panel.

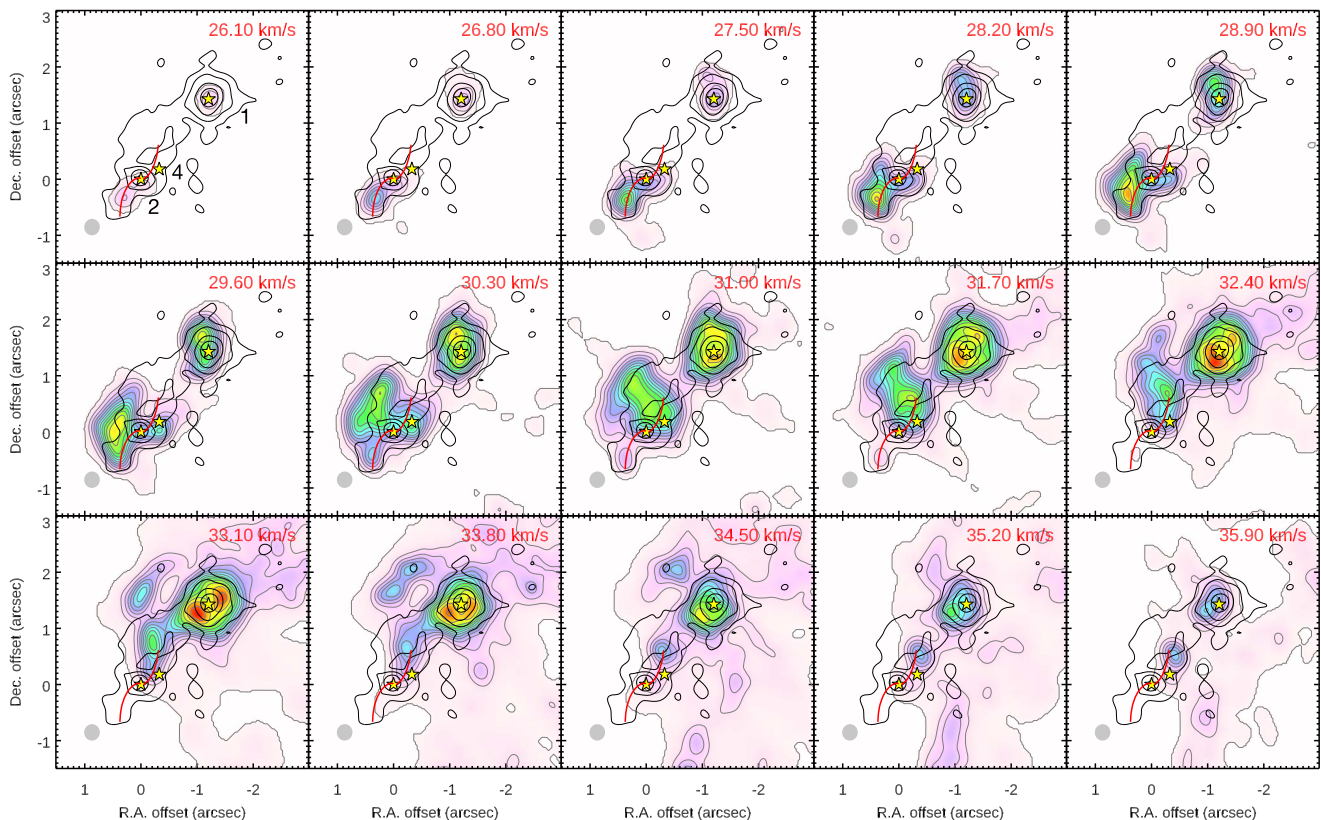


Figure 14. Same as Figure 13, but for the CH₃OH (4_{2,2} – 3_{1,2}; *E*) line. The gray contours start at 3 σ and have intervals of 6 σ (1 σ = 3.7 mJy beam⁻¹).

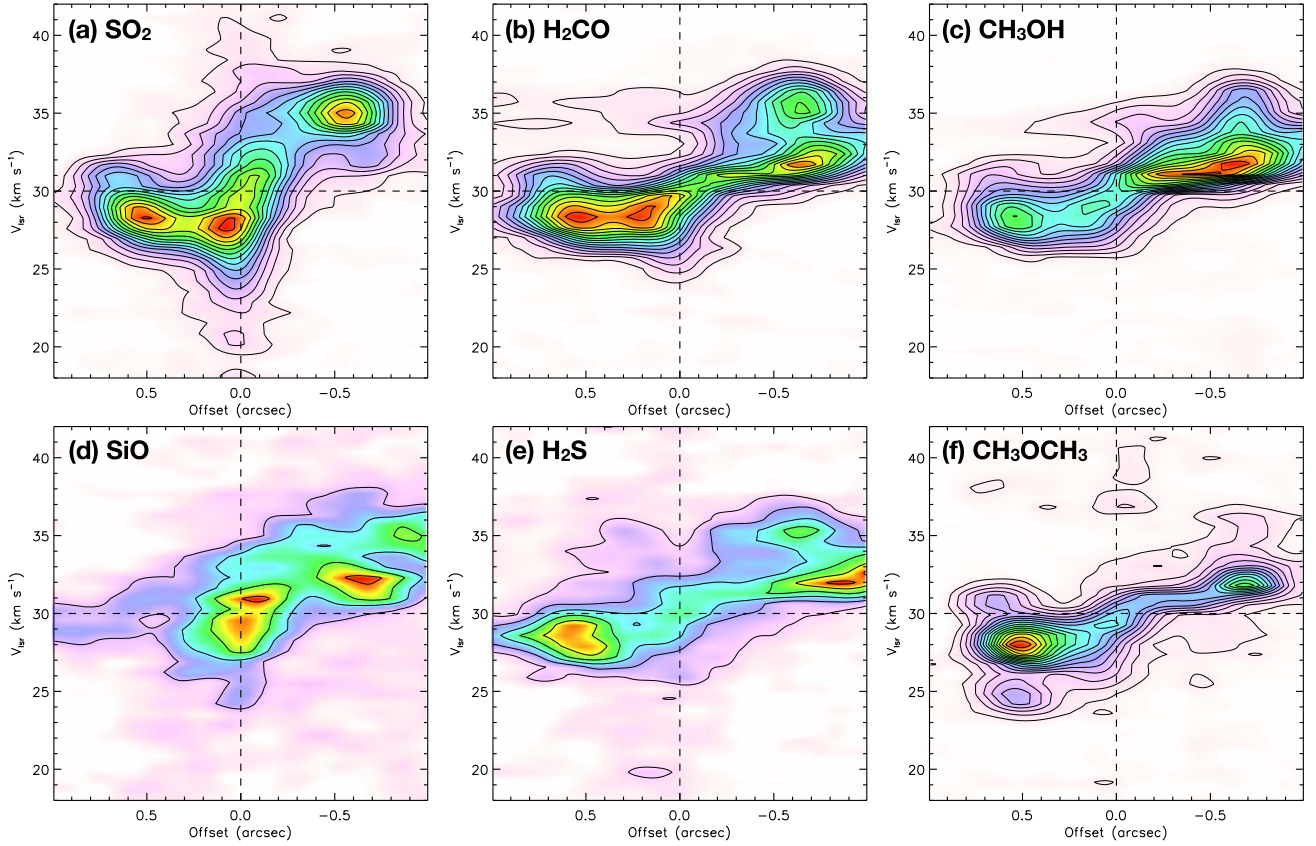


Figure 15. PV diagrams of the (a) SO_2 , (b) H_2CO , (c) CH_3OH , (d) SiO , (e) H_2S , and (f) CH_3OCH_3 emissions around source 2 along a cut with a position angle of $P.A. = -25^\circ$, i.e., the disk orientation obtained from the fit done by Sánchez-Monge et al. (2013), shown in color scales and black contours. The position offset is relative to the continuum peak position of source 2 identified from the C9 configuration data. The horizontal line indicates the systemic velocity of $V_{\text{sys}} = 30 \text{ km s}^{-1}$ of the source. The contours have the lowest level and intervals of 3σ , with $1\sigma = 3.2, 3.7, 4.5, 3.3, 3.2,$ and $2.6 \text{ mJy beam}^{-1}$ in panels (a)–(f), respectively.

kinematics of its proposed disk in these molecular lines. This position angle is consistent with the position angle of the disk derived from the previous 0.85 mm observation at a lower angular resolution (Sánchez-Monge et al. 2013). The spiral structures are also roughly aligned along this direction. Velocity gradients consistent with rotation are seen in all molecular lines. However, only in the SO_2 line, a high-velocity component reaching a rotation velocity of about 10 km s^{-1} is seen within about $0''.2$ (440 au) from the center. This high-velocity component is missing in all other molecular lines shown here. On the other hand, the low-velocity component of SO_2 is highly consistent with the other lines. The high-velocity inner component seen in the SO_2 line may be caused by an inner disk rotating faster.

There are two reasons why the SO_2 line can better trace the inner region and highlight the spiral structure. First, the observed SO_2 transition has a higher upper energy level ($E_u/k = 248 \text{ K}$) than the other lines shown here (see Table 4). Therefore it is more sensitive to the warmer inner region while the other molecular lines are more dominated by the outer cooler area. Second, as a typical shock tracer, the SO_2 emission may be enhanced by shocks associated with the spiral arms, and therefore more concentrated along the spiral arms than in the other species. Such behavior is very similar to what has been reported in several other massive protostellar disks, such as G339.88-1.26 (Zhang et al. 2019b) and IRAS16547-4247 (Tanaka et al. 2020). In those cases, SO_2 lines are also found to trace the inner region in the disk/envelope system with faster

rotation than molecular lines such as CH_3OH and H_2CO . However, in those sources, SiO emission is found to trace the innermost part of the disk with the highest rotation velocities, which is not seen in the case of G35.2.

6.1.2. Fitting the Spiral Structures around Source 2

To better understand the properties of the spiral structure seen in the SO_2 line, we fit them with two spiral shapes; one is a logarithmic spiral with the form of $R = R_0 e^{b\theta}$, and another is an Archimedean spiral with the form of $R = R_0 + b\theta$ (e.g., Huang et al. 2018; Kurtovic et al. 2018).

Figure 16(a) shows the integrated SO_2 emission in terms of distance from source 2 and polar angle. We determine the polar angle of the two spiral arms by their emission peaks at each distance on the emission polar map. Only the radius range between $0''.2$ and $0''.8$ is used as the spiral structure is most clear in this range. Figure 16(b) shows the fit to the determined spiral shapes. The parameters of the best-fit shapes are listed in Table 5. The pitch angles of the spirals $\phi = \tan^{-1}(\frac{dR}{Rd\theta})$ are also listed. It appears that the logarithmic shape fits the spiral arms better than the Archimedean shape, reproducing the curved shape (also see Table 5). The pitch angle is 69° for the NW arm and 62° for the southeast (SE) arm. Note that the two spiral arms lie along the major axis of the disk, the large pitch angles are partly due to the high inclination (closer to edge-on view) and the low spatial resolution.

There are commonly two mechanisms to form the spiral structures in a disk, gravitational instability and perturbation by

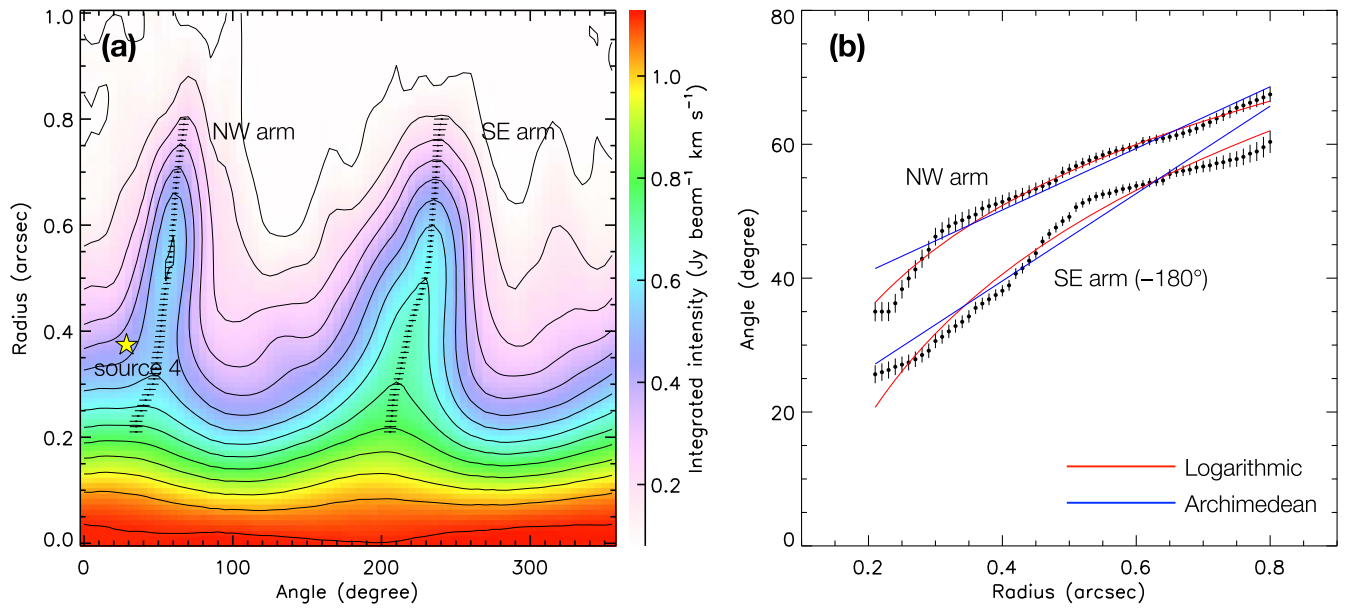


Figure 16. (a) Distribution of the SO_2 integrated emission in the space of radius from ALMA source 2 and polar angle. The yellow star marks the location of source 4. For each radius between $0''.2$ and $0''.8$ where the spiral structures can be well defined, the polar angles of the emission peaks of the two spirals are determined (data points). The errors (shown in 3σ levels) are determined by the beam size, radius, and the S/N, following $\Delta\theta = \theta_{\text{beam}}/(2r S/N)$, where $\theta_{\text{beam}} = 0''.3$ and r is the radius (distance to source 2). (b) Fits to the spiral structures in the SO_2 integrated emission map around ALMA source 2. The polar angle of the SE arm is rotated by 180° to compare with the NW arm. Each spiral structure is fitted with a logarithmic spiral (red curve) and an Archimedean spiral (blue curve).

Table 5
Parameters of the Best-fit Spirals

Spiral Arm	Logarithmic ($R = R_0 e^{b\theta}$)				Archimedean ($R = R_0 + b\theta$)			
	R_0 (arcsec)	b (deg^{-1})	Pitch Angle ^a (deg)	χ^2	R_0 (arcsec)	b (arcsec deg^{-1})	Pitch Angle (deg)	χ^2
NW	0.042	0.044	69°	0.77	-0.69	0.022	$81^\circ\text{--}57^\circ$	57
SE	0.00032	0.032	62°	3.9	-2.96	0.015	$78^\circ\text{--}48^\circ$	48

Note.

^a Pitch angle from $0''.2\text{--}0''.8$.

a companion or a planet (e.g., Forgan et al. 2018; Huang et al. 2018). A pair of symmetric logarithmic spiral arms are expected if the spiral structures are formed due to gravitational instability in the disk (e.g., Forgan et al. 2018). Also, the disk around source 2 is estimated to be about $3 M_\odot$ (Sánchez-Monge et al. 2013), which is relatively massive with respect to the mass of the central sources (sources 2 and 4 have a dynamical mass of about $18 M_\odot$ in total; see Section 5.5). Such a massive disk is prone to gravitational instability. Another possibility is that the spiral structures are caused by the perturbation of the binary companion, i.e., source 4. There are also several lines of evidence supporting such a scenario. First, the NW spiral arm shows a local minimum close to the location of source 4 (see Figure 16(a)), which may indicate that the binary companion has opened a gap in the spiral. Furthermore, despite that a single Archimedean spiral cannot well fit the NW arm, this can be fit with two Archimedean shapes with a discontinuity at $r \approx 0''.3$, which leads to a local maximum of pitch angle. In fact, simulations have shown that the spirals formed by perturbation of a companion have an increasing pitch angle toward the position of the companion (e.g., Zhu et al. 2015; Bae & Zhu 2018), which is similar to what we observed in the NW arm. Therefore, with the current data, it is difficult to

determine unambiguously which is the formation mechanism of the spiral structures in the source 2 disk.

However, it is also possible that the rotation structure around source 2 on the 2000 au scale is not truly a disk. The extent of the spiral structures (~ 2000 au) is much larger than the size of typical Keplerian disks around massive protostars seen in high-resolution observations, which have typical radii \lesssim a few $\times 10^2$ au (e.g., Ginsburg et al. 2018; Ilee et al. 2018; Zhang et al. 2019a; Maud et al. 2019). Furthermore, although the kinematics of the rotation structure around source 2 was explained by Keplerian rotation with lower-resolution data (Sánchez-Monge et al. 2013), its kinematics can also be explained by rotating-infalling material in the outer part feeding an inner small disk (see Figure 15). The high-velocity component shown in the SO_2 PV diagram (Figure 15(a)) has a radius of ~ 500 au, which is more consistent with other Keplerian disks in massive star formation. If this is the case, the spiral structures can be the infalling streamers feeding the inner disk. Such streamers on several $\times 10^3$ au scales were reported in other sources (e.g., Pineda et al. 2020), and can be explained by accretion of unsmooth turbulent material or even cloudlets (e.g., Kuffmeier et al. 2019; Hanawa et al. 2022). However, it is unclear whether such a scenario can explain the high symmetry seen in the pair of spiral structures.

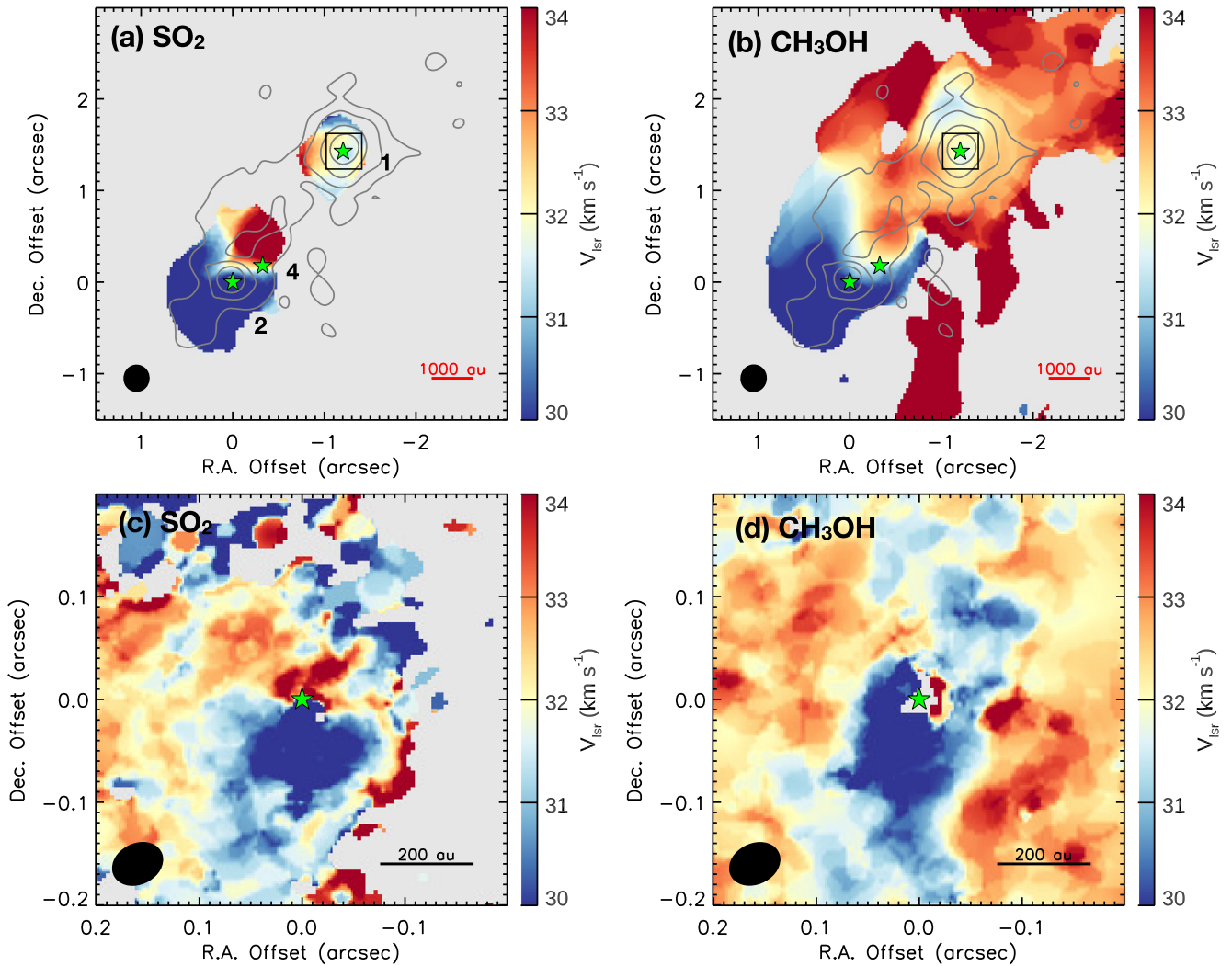


Figure 17. (a) Moment 1 map of the SO_2 ($22_{2,20} - 22_{1,21}$) emission shown in color scale, overlaid by the continuum emission shown in gray contours. The three stars mark the positions of sources 1, 4, and 2. The square indicates the region shown in panel (b). (b) same as panel (a), but for the CH_3OH ($4_{2,2} - 3_{1,2}; E$) line. (c) A zoom-in view of the moment 1 map of the SO_2 emission around source 1 (marked with the star). Data combining C3, C6, and C9 configurations are used. (d) Same as panel (c), but for the CH_3OH ($4_{2,2} - 3_{1,2}; E$) line.

6.1.3. Velocity Structure around Source 1

Rotation velocity gradients are also seen around source 1. In the low-resolution images, the emission around source 1 appears to be blueshifted in the NW and redshifted in the SE, opposite from that around source 2 (see Figure 17). Similar velocity gradient directions were reported by Sánchez-Monge et al. (2014) with ALMA 0.85 mm observations. However, with higher resolution, the innermost region ($<0''.1$, ~ 200 au) around source 1 shows a different velocity gradient direction, as shown by panels (c) and (d) in Figure 17. The innermost SO_2 emission is blueshifted in the south and redshifted in the north. The CH_3OH line has blueshifted emission in the SE. There is some redshifted emission in the NW of source 1 in the innermost region, but is affected by absorption. The velocity gradients in the innermost region around source 1 revealed by these two molecules are opposite from that in the outer region but generally consistent with that seen around source 2. This rotation direction is also consistent with the relative velocities of sources 1 and 2, as source 1 (the NW source) is redshifted with respect to source 2.

Figure 18 shows PV diagrams of SO_2 and CH_3OH lines, along a direction with a maximum velocity gradient across source 1 seen in the SO_2 moment 1 map (P.A. = 0°). In the SO_2 PV diagram, there are higher-velocity components with clear gradients in the innermost region that can be explained by rotation. However, in the case of pure rotation (e.g., a Keplerian disk), the blueshifted emission would be limited to one side while the redshifted emission would be limited to the other side, which is not compatible with the observed pattern. Instead, a combined motion of infall and rotation can reproduce the observed kinematics. Compared to the SO_2 emission, the CH_3OH emission shows a similar increase in velocity gradient toward the center. However, it does not show the central high-velocity component as SO_2 , indicating that the CH_3OH traces slightly outer regions than SO_2 , similar to the case of source 2 (Section 6.1.1). The CH_3OH line shows strong absorption against the bright continuum emission in redshifted velocities (see Figure 18(b)). This indicates infalling material in front of the central source along the line of sight, consistent with a combined motion of infall and rotation. Furthermore, if the accreting material is not evenly distributed (e.g., there are

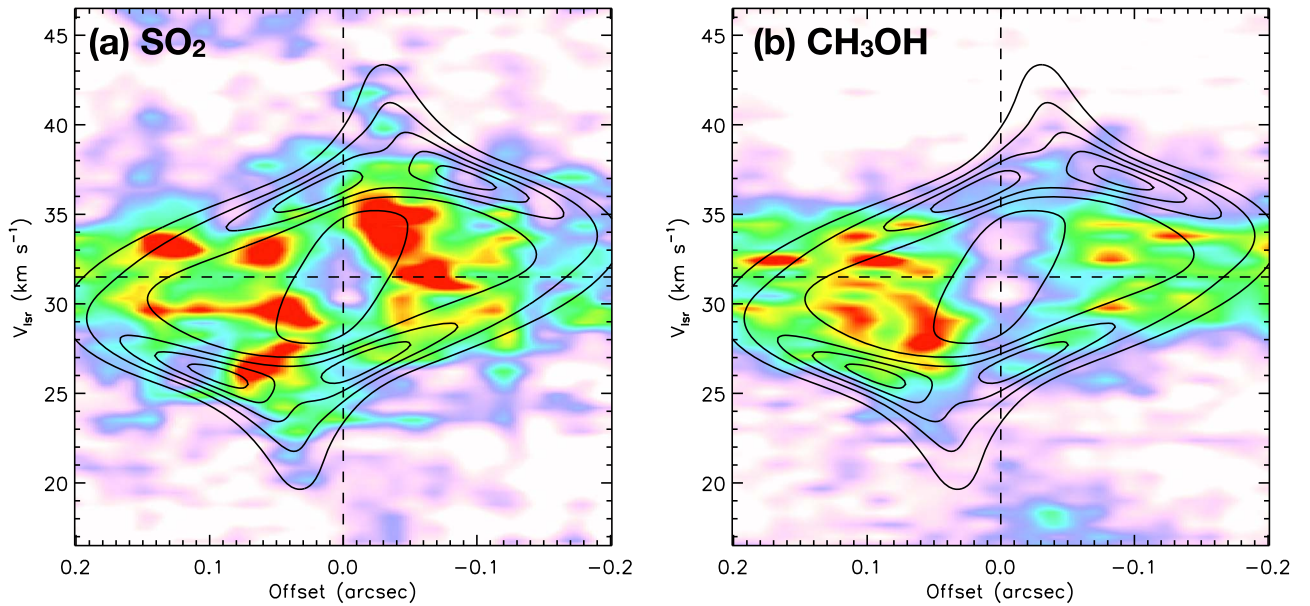


Figure 18. (a) PV diagram of the SO₂ line along a direction with maximum velocity gradient across source 1 (P.A. = 0°, the positive offset is toward the south). The combined data of C3, C6, and C9 configurations are used. The black contours show the model of an infalling-rotating envelope (see the text). (b) Same as panels (a) and (b), but for the CH₃OH (4_{2,2} – 3_{1,2}; E) line. The contours show the same model for the SO₂ emission.

unsmooth accretion flows), the combined motion of infall and rotation can cause the change of velocity gradient directions from the outer region to the inner region (e.g., Liu 2017).

To demonstrate the possibility of the combined motion of infall and rotation, we construct a simple model to fit the observed PV diagrams. Following the method used by Sakai et al. (2014a) and Zhang et al. (2019a), we fit the observed PV diagrams with a simple model of infalling rotation with the rotation velocity v_φ and infall velocity v_r described as

$$v_\varphi(r) = v_{\text{CB}} \frac{r_{\text{CB}}}{r}, \quad (1)$$

$$v_r(r) = -v_{\text{CB}} \frac{\sqrt{r_{\text{CB}}(r - r_{\text{CB}})}}{r}. \quad (2)$$

Such motion conserves both angular momentum and mechanical energy. r_{CB} is the innermost radius that such infalling gas can reach with the angular momentum conserved (i.e., the centrifugal barrier), where $v_\varphi = v_{\text{CB}}$ and $v_r = 0$. v_{CB} is the rotational velocity at the centrifugal barrier. In such a model, the central mass is $m_* = r_{\text{CB}} v_{\text{CB}}^2 / (2G)$. Since we only focus on the kinematics pattern here, we adopt a simple geometry and density distribution in the model. We assume the disk has a height of $h(r) = 0.2r$ on each side of the midplane, and the density distribution follows $\rho(r) \propto r^{-1.5}$ (e.g., Oya et al. 2016). For simplicity, we also assume the emissions are optically thin and the excitation conditions are uniform across the region. Note that the density distribution, excitation conditions, and disk height profiles have a combined effect on the detailed emission pattern, but do not affect the general kinematics pattern, which we aim to explore here. We also fix the outer radius to be 0''.2 (4.4×10^2 au), as we only focus on the kinematics of the innermost region. Therefore, we have in total three free parameters: the central mass m_* , the radius of the centrifugal barrier r_{CB} , and the inclination angle i .

To obtain the best-fit model, we compare the model PV diagram with the observed PV diagram of the SO₂ line. We

focus on the SO₂ line as the CH₃OH line does not trace the innermost region well. We explore the inclination angle i with values ranging from 0° to 40° with an interval of 10°, the angular radius of the centrifugal barrier r_{CB}/d in a range of 0''.01–0''.05 with an interval of 0''.01, and the central dynamical mass in a range of 4–12 M_\odot with an interval of 1 M_\odot , and approximately determine the best-fit model by eye. The SO₂ PV diagram can be well reproduced by the model with $r_{\text{CB}}/d = 0''.03$ ($r_{\text{CB}} \approx 70$ au), $i = 30^\circ$ between the line of sight and the disk midplane, $m_* = 6 M_\odot$ (Figure 18(a)). In Figure 18(b), we show a comparison of this model and the CH₃OH emission. The CH₃OH emission is consistent with the model in the outer part, but does not show the innermost high-velocity component. This confirms the scenario that CH₃OH traces a region with slightly larger radii than that traced by the SO₂ emission.

Our model fitting shows that infalling rotation can be a viable explanation for the gas kinematics in the innermost region around source 1. We note that we cannot rule out all the other possibilities. Especially, our data have limited sensitivities for the extended emissions, and the rotation direction changes from larger scale to the small scale, therefore our simple model cannot model the kinematics of more extended emission. Nevertheless, the model fitting suggests that the rotating structure around source 1 is not rotationally supported. The derived central mass of 6 M_\odot is close to that estimated from the ionizing photon rate (see Section 5), and higher than the previously derived dynamical mass of 4 M_\odot (Sánchez-Monge et al. 2014). In the previous estimation, a Keplerian disk was assumed, higher dynamical mass is expected if the disk is not rotationally supported. Despite the non-detection of the rotationally supported disk in our observation, such a disk may exist inside the centrifugal barrier, i.e., within a radius of 0''.03 (~ 70 au). The resolution and line coverage of our current observation may not be able to effectively probe such a disk.

Overall, the hierarchical accretion structure around sources 1 and 2, in which both sources are fed by a common rotating structure, and each of them is fed by the individual rotating structure, indicates that the accretion toward these two sources

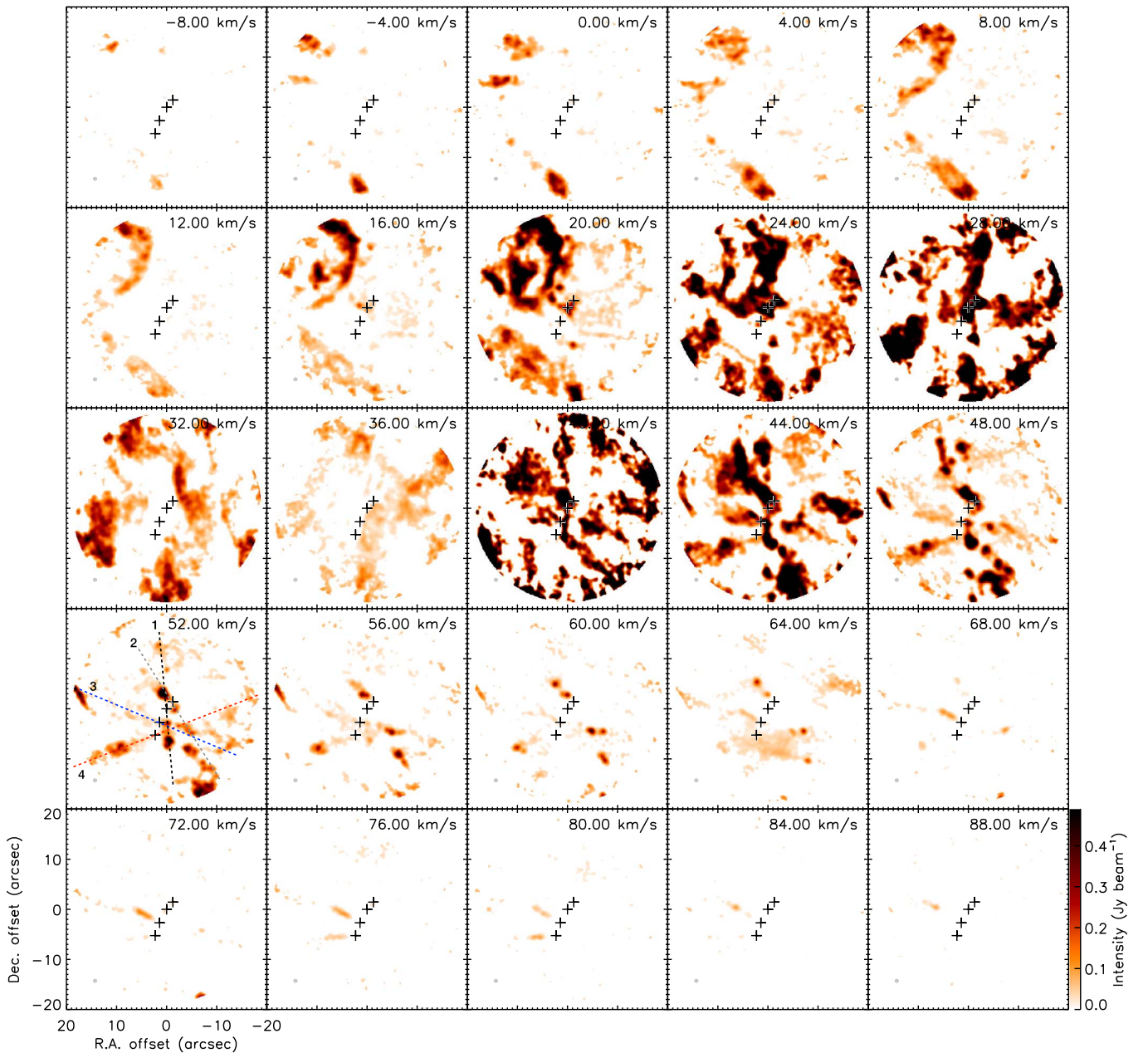


Figure 19. Channel maps of the ^{12}CO (2-1) line. Each channel has a width of 4 km s^{-1} . The central velocity of each channel is labeled in each panel. Only the C3 configuration data are used, and the synthesized beam is shown in the lower-left corner of each panel. The dashed lines in the channel of $V_{\text{lsr}} = 52 \text{ km s}^{-1}$ show the directions of the identified four outflow components. The four crosses mark the four sources that we identify as the driving sources of these outflow components. From north to south (N–S), the four sources and their associated cores are source 1 (core A), source 2 (core B), source 14 (core C), and source 17 (core E).

is still highly active and the start of photoionization has not stopped the accretion.

6.2. Molecular Outflows

Figure 19 shows the ^{12}CO channel maps of G35.2. The ^{12}CO emission shows a complex morphology. Our short observations with limited $u-v$ coverage cannot effectively recover the extended component of the emission, causing significant missing flux, which makes it even more difficult to analyze the outflows in this region.

In the blueshifted velocities (with respect to the systemic velocity, which is around $V_{\text{lsr}} = +30$ to $+35 \text{ km s}^{-1}$; see Section 6.1), the most distinguishable outflow feature is a wide arc-shaped structure toward the NE. This feature is best

seen in velocity channels $V_{\text{lsr}} \lesssim +16 \text{ km s}^{-1}$, but can also be seen in less blueshifted velocities down to $V_{\text{lsr}} = +24 \text{ km s}^{-1}$. The wide-angle CO outflow toward the NE has been seen in previous observations, including single-dish observations (e.g., Gibb et al. 2003; Birks et al. 2006). This structure is also seen in the NIR both in molecular and atomic emission (Caratti o Garatii et al. 2015; Fedriani et al. 2019). On the other hand, in the redshifted velocity channels, the emission appears to be more concentrated in a few collimated components, which are better shown in the integrated emission map shown in Figure 20. We identify in total four collimated outflow components, which are labeled by dashed lines with different colors in Figure 19 (in the channel of $V_{\text{lsr}} = +52 \text{ km s}^{-1}$) and Figure 20. Assuming that they are separate outflows, we

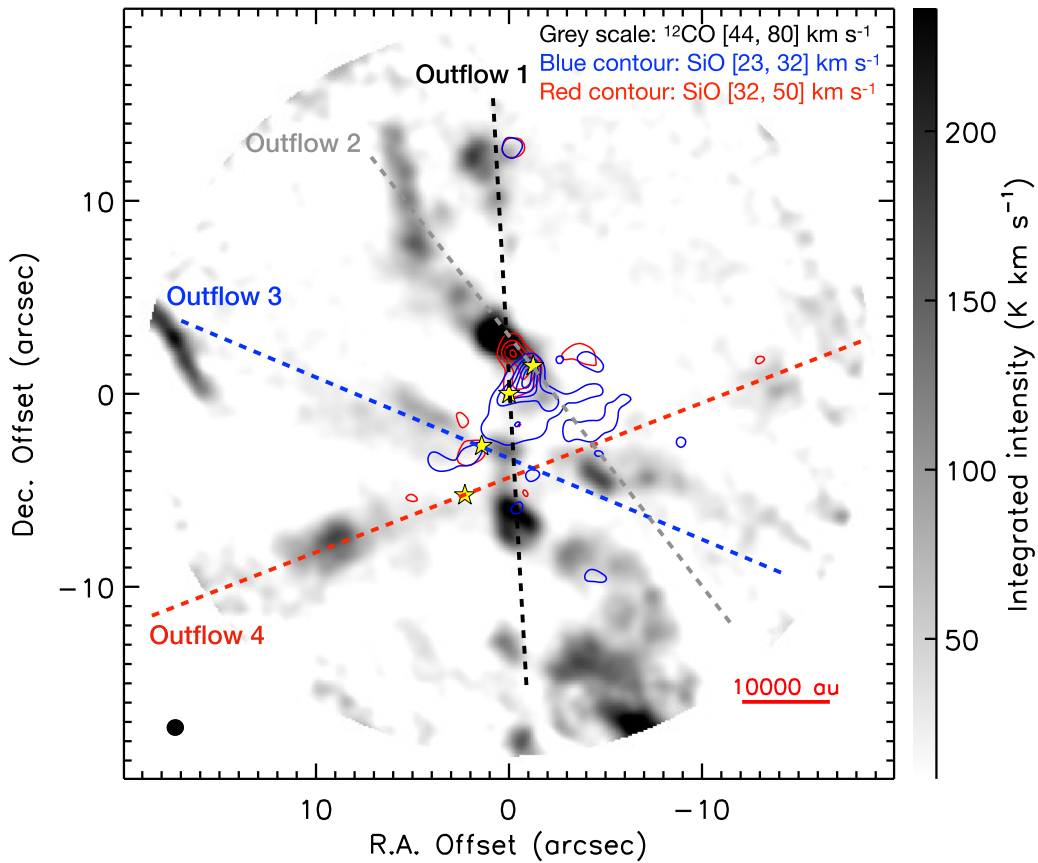


Figure 20. Integrated map of the ^{12}CO (2-1) line shown in grayscale, overlaid with integrated maps of the blueshifted and redshifted SiO emission shown in blue and red contours, respectively. The integrated velocity ranges of the lines are shown in the upper-right corner of the figure. The dashed lines show the directions of the identified four outflow components (same as those in the channel of $V_{\text{lsr}} = 52 \text{ km s}^{-1}$ in Figure 19). The four crosses mark the four driving sources. From N–S, the four sources and their associated cores are source 1 (core A), source 2 (core B), source 14 (core C), and source 17 (core E).

identify their driving sources by comparing their locations with the positions of the continuum sources.

Outflow 1 (marked with the black dashed line) is most clearly seen in the channels of $+40 \text{ km s}^{-1} \leq V_{\text{lsr}} \leq +52 \text{ km s}^{-1}$, but it can also be seen in slightly blueshifted channels of $V_{\text{lsr}} = +28 \text{ km s}^{-1}$. At $V_{\text{lsr}} = +48 \text{ km s}^{-1}$, it is clear that there is a string of bright CO blobs associated with this outflow. Despite the fact that this outflow component does not have a well-defined structure in our data, we believe it traces the same N–S outflow component identified in previous CO observations (e.g., Birks et al. 2006), and is consistent with the radio jet (Gibb et al. 2003; Beltrán et al. 2016) and the bright outflow cavity seen in the NIR to MIR (De Buizer 2006; Zhang et al. 2013; Fedriani et al. 2019). This outflow appears to originate from source 2 (core B).

There appears to be an outflow associated with source 1 (core A), which is most clearly seen as two bright blobs to the NE of source 1 at velocities $+56 \text{ km s}^{-1} \leq V_{\text{lsr}} \leq +64 \text{ km s}^{-1}$. This outflow has a position angle of about 30° , if the blobs toward the opposite direction are also associated with it (marked with the gray dashed line in Figures 19 and 20). This outflow is also traced by the SiO emission (Figure 20), which is best seen as a high-velocity redshifted emission blob (up to $V_{\text{lsr}} > +50 \text{ km s}^{-1}$) originating from source 1 in the same direction as the ^{12}CO outflow. This SiO outflow has been reported by Sánchez-Monge et al. (2014). Its blueshifted emission is more extended and mostly resides along the filamentary continuum structure. It is possible that, in addition

to the outflow, the SiO emission also traces the shocks caused by the gas flows forming the filament.

Outflow 3 (marked with the blue dashed line) originates from source 14 (core C). It is clearly seen at velocities $V_{\text{lsr}} \geq +48 \text{ km s}^{-1}$. To the NE of source 14, there is a high-velocity component in this outflow that can be seen from $V_{\text{lsr}} = +68 \text{ km s}^{-1}$ up to $V_{\text{lsr}} > +90 \text{ km s}^{-1}$. This outflow has a position angle of 70° . The position angles of outflows 2 and 3 are highly consistent with the two larger-scale outflows seen in NIR shocked H_2 emission (Caratti o Garattii et al. 2015). Therefore, they are likely the same outflows seen in different wavelengths and different tracers. If this is the case, the wide CO outflow toward the NE should be a combination of these two outflows rather than a single wide outflow. Furthermore, if these two outflows are driven by sources 1 and 15, they are separated from the N–S outflow (outflow 1) driven by source 2. This suggests that the large NE outflow is not caused by the precession of the N–S outflow/jet, but rather, they are independent outflows driven by different sources.

Finally, we identify a fourth outflow (marked by a red dashed line in Figure 19) at a position angle of 110° originating from source 17 (core E). This outflow is best seen to the east of source 17 at velocities of $+48 \text{ km s}^{-1} \leq V_{\text{lsr}} \leq +60 \text{ km s}^{-1}$, but can also be seen at high outflowing velocities ($V_{\text{lsr}} = +80 \text{ km s}^{-1}$, with a slightly different position angle). This outflow has not been reported by previous studies.

Note that outflows 3 and 4 are only seen clearly in the high-velocity redshifted channels. The crowded nature of this region,

as well as the fact that the observation is very shallow with a lot of missing flux and side-lobe effects, make it very difficult to identify the different outflow structures in all the velocity channels. Therefore, with the current data, it is hard to conclude if the corresponding blueshifted components of outflows 3 and 4 are really missing or they are not seen because of the observation difficulties.

7. Lower-mass Members of the Cluster

As presented in Section 3, we identify 22 compact sources from the ALMA long-baseline continuum image. As discussed in Section 5, the emission from 6 cm to 1.3 mm in sources 1–3 suggest that they are massive young stars that have created small photoionized regions around them. A similar scenario may be also true for source 4, but it can also be a low-mass protostar with a shock-ionized region caused by jet activity. Other sources are assumed to be low-mass members in the forming cluster. Following previous similar studies (e.g., Plunkett et al. 2018; Busquet et al. 2019), we use several methods to characterize their distribution.

We assume that the detected long-baseline (C9) 1.3 mm dust continuum emission in these sources comes from their disks and/or inner envelope (referred to as disks for simplicity), and therefore use the continuum fluxes to estimate the masses of such structures of the sources using the following equation:

$$M = \frac{d^2 F_{\text{dust}, 1.3\text{mm}}}{\kappa_{1.3\text{mm}} B_{1.3\text{mm}}(T_{\text{dust}})}, \quad (3)$$

where $d = 2.2$ kpc is the distance to the source, $F_{\text{dust}, 1.3\text{mm}}$ is the estimated dust continuum emission flux, and $B_{1.3\text{mm}}(T)$ is the Planck function. An opacity of $\kappa_{1.3\text{mm}} = 0.00899 \text{ cm}^2 \text{ g}^{-1}$ is used (Ossenkopf & Henning 1994; for MRN dust with thin ice mantles and gas density of 10^6 cm^{-3} ; a gas-to-dust mass ratio of 100 is assumed). The disk masses are listed in Table 2. For sources 1–4 (massive sources), a dust temperature of 100 K is assumed (suitable for typical massive sources; e.g., Zhang et al. 2014), and for sources 5–22, a dust temperature of 30 K is assumed (e.g., Tobin et al. 2013). Note that for sources 1–4, the free-free component estimated from modeling the SEDs and HRL fluxes (see Section 5) has been subtracted from the continuum fluxes. As the continuum fluxes are estimated with only the long-baseline image, the larger filament or accretion structure is filtered out, i.e., only the individual disk (and/or inner envelope) of each source is included in the mass estimation. Based on the assumed dust opacity, gas-to-dust ratio, and dust temperature of 30 K, the column density sensitivity is 6.3 g cm^{-2} at the center of the field of view, which corresponds to a mass sensitivity of $3.8 \times 10^{-3} M_{\odot}$ for unresolved sources.

Figure 21(a) shows disk masses as a function of the projected distance from massive stars. Here, for any source, we calculate its distances to sources 1 and 2, and use the smaller value as its distance from massive stars. It appears that the sources within a distance of 3000 au of the massive stars have relatively low disk masses. Such a trend can be explained by the depletion of disks in the regions close to the massive stars. It may be due to the tidal/dynamic interactions between the sources in such a crowded region. In fact, our molecular line observations have revealed complex accretion structures on multiple scales that fit such a scenario (see Section 6.1).

Another possibility of disk depletion close to the massive stars is photoevaporation by high UV radiation. However, this is less likely to be the main cause in our case. As discussed in Section 5, the massive sources in this cluster have not yet developed large H II regions, and are still highly embedded inside dense disk/envelope structures. However, such a trend may be caused by other effects. Many of the sources close to the massive stars are associated with the larger filament and the hierarchical accretion structures (see Section 6.1). The long-baseline observations detect the small over-densities inside the larger structures associated with these sources. Whether such over-densities can represent the individual circumstellar disks is uncertain.

Figure 21(b) shows the distribution function of the projected separations between pairs of sources in the cluster. We calculate the distribution function $p(s)$ by counting the number of pairs (N_i) with separation in the interval of $(s, s + \Delta s)$, normalized by the total pair number (e.g., Cartwright & Whitworth 2004; Busquet et al. 2019)

$$p(s) \Delta s = \frac{2N_i}{N_{\text{tot}}(N_{\text{tot}} - 1)}, \quad (4)$$

where $N_{\text{tot}} = 22$ is the total source number. Here, the separation s is normalized to the cluster radius $r_{\text{max}} = 18''1$ (4.0×10^4 au), which is determined by the maximum separation between any source to the average position of all the sources. The distribution function shows a single peak at about $5''$ (normalized $s \approx 0.25$). As demonstrated by Cartwright & Whitworth (2004), a single peak in the distribution function is consistent with a smooth radial gradient of source density without subclustering. With $N_{\text{tot}} = 22$ and $r_{\text{max}} = 4.0 \times 10^4$ au, this cluster has a number density of protostellar sources of $n = 7.2 \times 10^2 \text{ pc}^{-3}$. There are 20 sources within 2.5×10^4 au (primary beam response > 0.5), which yields a number density of $n = 2.7 \times 10^3 \text{ pc}^{-3}$.

We further use the minimum spanning tree (MST) method to characterize the clustering of these sources (Figure 21(c)). It shows the shortest path length connecting all the sources without including closed loops (Kruskal 1956). We construct the MST using the python package NetworkX (Hagberg et al. 2008). Following Cartwright & Whitworth (2004), from the constructed MST, we derive the Q parameter, which is used to distinguish between a smooth overall radial density gradient and multi-scale fractal subclustering. The Q parameter is defined as $\bar{Q} \equiv \bar{m}/\bar{s}$, where \bar{m} is the mean MST path length normalized by the factor $\sqrt{N_{\text{tot}}A}/(N_{\text{tot}} - 1)$ with $A = \pi r_{\text{max}}^2$ being the cluster area, and \bar{s} is the mean separation of all the sources normalized to the cluster radius. From $\bar{m} = 0.40$ obtained from MST, and $\bar{s} = 0.43$ from the separation distribution (Figure 21(b)), we have $\bar{Q} = \bar{m}/\bar{s} = 0.95$. $\bar{Q} = 0.8$ is considered as a diagnostic boundary; higher values indicate a smooth overall radial density gradient and lower values indicate a fractal subclustering (Cartwright & Whitworth 2004). The result of $\bar{Q} = \bar{m}/\bar{s} = 0.95$ is consistent with a cluster without subclustering, as the observed single-peaked separation distribution function has suggested.

Based on the MST method, we further calculate the mass segregation ratio Λ_{MSR} following the definition by Allison et al. (2009)

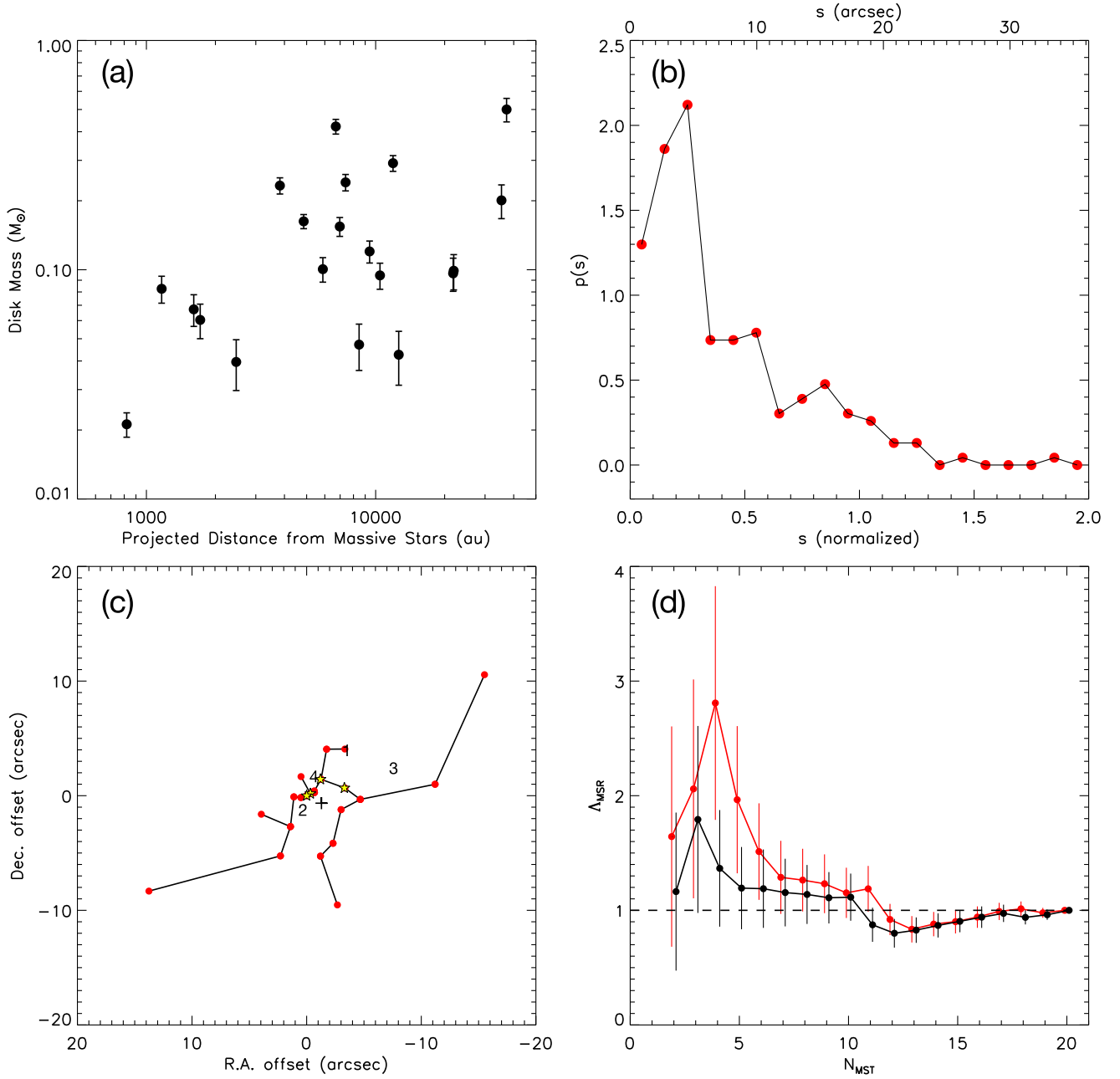


Figure 21. (a) Disk mass (estimated from the total dust continuum flux) of the compact sources detected with ALMA long-baseline observations (see Table 2) as a function of their projected distances from the massive stars. Here, for any source, we calculate its distances to sources 1 and 2, and use the smaller value as its distance from massive stars. For sources 1–4, free-free emission is subtracted from the continuum (see Table 2 and Section 5). (b) Distribution function of separations between the ALMA sources. The quantity $p(s)\Delta s$ (area under the curve) is the number of pairs of sources with their separation falling within the range $[s, s + \Delta s]$. Separation s is normalized to the cluster radius ($18''1, 4.0 \times 10^4$ au), which is determined by the maximum separation between any source to the average position of all the sources. (c) MST for the ALMA sources. The position offsets are with respect to the position of source 2. The stars mark the four massive sources with corresponding VLA detection (sources 1–4). The cross marks the average position of all the sources. (d) Mass segregation ratio parameter Λ_{MSR} (see text) as a function of the number of most massive sources. The black data points and curve show Λ_{MSR} calculated with sources ordered by their disk masses. The red data points and curve show Λ_{MSR} calculated by setting the four sources with VLA detections (sources 1–4) to be the most massive ones (ordered by their estimated stellar mass), followed by the other sources ordered by their disk masses. The two outermost sources are not included as the low primary beam response near the edge of the field of view biases toward relatively bright and therefore massive sources. The two sets of data points are offset slightly on the x -axis for better presentation. The dashed line shows $\Lambda_{\text{MSR}} = 1$ indicating no mass segregation.

$$\Lambda_{\text{MSR}} = \frac{L_{\text{norm}}}{L_{\text{massive}}} \pm \frac{\sigma_{\text{norm}}}{L_{\text{massive}}}, \quad (5)$$

where L_{massive} is the path length of the MST of the N most massive sources. L_{norm} and σ_{norm} are the average path length and its statistical deviation of the MST of N sources randomly

selected from the cluster. To estimate L_{norm} and σ_{norm} , we randomly select 500 sets of sources for each N (Allison et al. 2009; Plunkett et al. 2018). Note that we exclude the outermost two sources from this analysis, as the low primary beam response near the edge of the field of view strongly biases against dimmer and therefore less massive sources.

Figure 21(d) shows Λ_{MSR} as a function of the number of most massive sources in the cluster used in constructing the MST analysis (N_{MST}). A value of $\Lambda_{\text{MSR}} = 1$ indicates a random distribution of sources without mass segregation, and $\Lambda_{\text{MSR}} > 1$ suggests that the N most massive sources are more concentrated with respect to the random sample, i.e., a mass segregation. The black data points show Λ_{MSR} calculated with sources ordered by their disk masses. The mass segregation becomes significant only for the most massive three sources and peaks at $N_{\text{MST}} = 3$, which corresponds to sources 1 and 2. However, for sources 1–4, the level of dust continuum emission is uncertain because the estimation of free–free contamination depends on the model (see Section 5). Meanwhile, these four sources should be the most massive sources as they have already formed photoionized regions. The red data points show Λ_{MSR} calculated by setting these four sources to be the most massive ones (ordered by their estimated stellar mass), followed by other sources ordered by the estimated disk masses. In this case, Λ_{MSR} clearly has a peak at $N_{\text{MST}} = 4$ indicating that these four massive sources show strong segregation from the other members of the cluster. No strong mass segregation is seen for $N_{\text{MST}} \gtrsim 6$, which corresponds to $m_{\text{disk}} < 0.16 M_{\odot}$. Considering the short formation timescale of massive stars and the fact that the photoionized regions of most massive sources in this cluster are still highly compact, the mass segregation is unlikely to be caused by dynamical relaxation (as is the case for more evolved clusters). However, instead, it should reflect the primordial mass segregation during the formation of the massive protostellar cluster.

8. Summary

We have presented ALMA 1.3 mm intermediate-resolution and long-baseline observations toward the massive star-forming region G35.20-0.74 (G35.2). Using the continuum emission and emission from different molecular lines, we characterized the massive and low-mass protostars in the region and their accretion and outflow structures. Our main conclusions are as follows:

1. The 1.3 mm intermediate-resolution continuum image shows a string of cores along the filamentary structure, similar to what has been seen in the previous 0.85 mm observation. From the 1.3 mm long-baseline observation, we identified 22 compact continuum sources, suggesting a young forming cluster in the region. Among them, four sources have corresponding VLA detections from 6 cm to 7 mm. Three of them (ALMA sources 1–3) are consistent with massive young stars that have initiated photoionization, while the other source (ALMA source 4) could be a low-mass protostar with shock-induced free–free emission. Furthermore, we report the detection of a compact source at the location of source 3 in the 0.85 mm continuum, found as a result of reprocessing previously published 0.85 mm continuum data. The other 18 sources without corresponding VLA detections are considered to be lower-mass members in the cluster.
2. Among the massive sources, two (sources 2 and 3) are found to have H30 α recombination line emission. The H30 α line kinematics shows ordered motions of the ionized gas in the innermost region. For source 3, the H30 α kinematics are consistent with disk rotation, while for source 2 it is more consistent with the outflowing

motion. We found evidence of potential maser activity in the H30 α line emission of source 3, adding another candidate case to the handful of millimeter HRL maser discovered so far.

3. We constructed models of photoionized regions to simultaneously fit the multiwavelength free–free fluxes and the H30 α total fluxes. The model assumes an isothermal ionized region with a power-law distribution in the emission measure (and electron density), so that it can fit the observed SEDs, which show partially optical thick free–free emission over wide frequency ranges. The derived properties of the ionized regions are consistent with photoionized HCH II regions.
4. Molecular line emission shows multi-scale accretion structures around sources 1 and 2 (cores A and B). We have inferred that sources 1 and 2 are surrounded by a common rotating structure that connects to the individual disks. The source 2 disk is found to have two spiral arms, which may be caused by gravitational instability or perturbation of the binary companion source 4. As another possibility, the spiral structures could also be infalling streamers feeding an inner unresolved disk in source 2. The spiral arms are best seen in the SO₂ emission, which is enhanced by shocks along the spirals. SO₂ also traces the inner faster-rotating part of the disk while other molecular lines such as CH₃OH and H₂CO only trace the outer slower-rotation part. The source 1 disk appears to be more compact than the source 2 disk and not rotationally supported. Its velocity structure is consistent with infalling rotation of unsmooth accretion flows. The existence of such multi-scale accretion structures feeding sources 1 and 2 suggests that the accretion is still going on and is not stopped by the photoionization feedback.
5. From the ¹²CO emission, we identified in total four outflows likely driven by four different sources (sources 1, 2, 14, and 17). By comparing with the outflows identified in previous studies with different tracers, we speculate that the N–S CO outflow driven by source 2 is consistent with the radio jet and the bright outflow cavity seen in NIR and MIR. The wide outflow toward the NE is actually composed of two separate outflows driven by source 1 and source 14, and it is not formed by the precession of the N–S jet. Furthermore, we identify another outflow in the east–west direction, driven by source 17.
6. We analyzed the distribution of the identified compact continuum sources in the cluster. Assuming the compact dust continuum emission associated with these sources comes from their disks or inner envelopes, we analyzed the relation of their masses with their distances to the massive stars, and found potential disk depletion due to dynamical interactions in the inner region. The spatial distribution of the sources suggests a smooth overall radial density gradient without subclustering, and tentative evidence of primordial mass segregation.

This paper makes use of the following ALMA data: ADS/JAO.ALMA#2015.1.01454.S, and ADS/JAO.ALMA#2017.1.00181.S. ALMA is a partnership of ESO (representing its member states), NSF (USA) and NINS (Japan), together with NRC (Canada), MOST and ASIAA (Taiwan), and KASI (Republic of Korea), in

cooperation with the Republic of Chile. The Joint ALMA Observatory is operated by ESO, AUI/NRAO and NAOJ. Y.Z. acknowledges support from RIKEN Special Postdoctoral Researcher Program and JSPS KAKENHI grant JP19K14774. K. E.I.T. acknowledges support by JSPS KAKENHI grant Nos. JP19K14760, JP19H05080, JP21H00058, JP21H01145. J.C.T. acknowledges support from ERC project MSTAR, VR grant 2017-04522. Y.-L.Y. acknowledges the support from the Virginia Initiative of Cosmic Origins (VICO) Postdoctoral Fellowship. R.F. acknowledges funding from the European Unions Horizon 2020 research and innovation program under the Marie Skłodowska-Curie grant agreement No. 101032092. G.G. acknowledges support by the ANID BASAL project FB210003.

Software: CASA (<http://casa.nrao.edu>; McMullin et al. 2007), The IDL Astronomy User's Library (<https://idlastro.gsfc.nasa.gov>), NetworkX (<https://networkx.org>; Hagberg et al. 2008).

Appendix

Model Fitting to the Continuum Spectrum and H30 α Emission

We construct a simple model to simultaneously fit the continuum flux densities observed in multiple VLA bands and ALMA 1.3 mm, as well as the total integrated flux density of the H30 α line.

The optical depth of the free-free emission (e.g., Wilson et al. 2013) is

$$\tau_{\nu,\text{ff}} = 8.235 \times 10^{-2} \left(\frac{T_e}{\text{K}} \right)^{-1.35} \left(\frac{\nu}{\text{GHz}} \right)^{-2.1} \left(\frac{\text{EM}}{\text{pc cm}^{-6}} \right). \quad (\text{A1})$$

where T_e is the temperature of the ionized gas, and EM is the emission measure defined as $\text{EM} \equiv \int n_e^2 dh$. Assuming that the ionized gas is isothermal, the radiative transfer of the free-free emission gives the brightness temperature as

$$T_{\nu,\text{ff}} = T_e (1 - e^{-\tau_{\nu,\text{ff}}}). \quad (\text{A2})$$

The total free-free flux density is then

$$S_{\nu,\text{ff}} = \frac{2k\nu^2}{c^2} \int T_{\nu,\text{ff}} d\Omega, \quad (\text{A3})$$

where Ω is the solid angle.

The optical depth of the HRL line center under LTE condition (e.g., Wilson et al. 2013) is

$$\tau_{\text{HRL},0} = 1.92 \times 10^3 \left(\frac{T_e}{\text{K}} \right)^{-5/2} \left(\frac{\text{EM}}{\text{pc cm}^{-6}} \right) \left(\frac{\Delta\nu}{\text{kHz}} \right)^{-1}. \quad (\text{A4})$$

For H30 α line (231.9 GHz), the line center optical depth (Equation (A4)) is

$$\tau_{\text{H30}\alpha,0} = 2.48 \left(\frac{T_e}{\text{K}} \right)^{-5/2} \left(\frac{\text{EM}}{\text{pc cm}^{-6}} \right) \left(\frac{\Delta\nu}{\text{km s}^{-1}} \right)^{-1}, \quad (\text{A5})$$

where $\Delta\nu$ and Δv are the FWHM of the line in the frequency and the velocity, respectively.

For a typical electron temperature of 10^4 K and typical HRL line width of 40 km s^{-1} , H30 α is optically thin except for extremely high emission measures ($\text{EM} > 1.6 \times 10^{11} \text{ pc cm}^{-6}$). Therefore, the brightness temperature of the *free-free continuum subtracted* from H30 α is

$$T_{\text{HRL}} = T_e e^{-\tau_{\text{ff}}} (1 - e^{-\tau_{\text{HRL}}}) = T_e e^{-\tau_{\text{ff}}} \tau_{\text{HRL}}. \quad (\text{A6})$$

Note that here the factor of $e^{-\tau_{\text{ff}}}$ includes the effects of the non-optically thin free-free continuum on the line intensity. From Equations (A5) and (A6), the integrated H30 α intensity is then

$$\left(\frac{\int T_{\text{H30}\alpha} dv}{\text{K km s}^{-1}} \right) = 2.64 \left(\frac{T_e}{\text{K}} \right)^{-3/2} \left(\frac{\text{EM}}{\text{pc cm}^{-6}} \right) e^{-\tau_{\text{ff}}}, \quad (\text{A7})$$

and the total H30 α flux density integrated over velocity and space is

$$S_{\text{H30}\alpha} = \frac{2k\nu^2}{c^2} \iint T_{\text{H30}\alpha} dv d\Omega. \quad (\text{A8})$$

Note that if the free-free and HRL emissions are optically thin, we have a line-to-continuum ratio of

$$\left(\frac{\int T_{\text{HRL}} dv}{T_{\text{ff}}} \right)_{\text{thin}} = \left(\frac{\tau_{\text{HRL},0}}{\tau_{\text{ff}}} \right) \Delta\nu \left(\frac{1}{2} \sqrt{\frac{\pi}{\ln 2}} \right) \quad (\text{A9})$$

$$= 7.445 \times 10^3 \text{ km s}^{-1} \left(\frac{T_e}{\text{K}} \right)^{-1.15} \left(\frac{\nu}{\text{GHz}} \right)^{1.1}. \quad (\text{A10})$$

For the H30 α line, we have

$$\left(\frac{\int T_{\text{H30}\alpha} dv}{T_{\text{ff}}} \right)_{\text{thin}} = 74.7 \text{ km s}^{-1} \left(\frac{T_e}{10^4 \text{ K}} \right)^{-1.15}. \quad (\text{A11})$$

The true line-to-continuum ratio should be lower than this if the free-free continuum is not optically thin, or higher than this if non-LTE effects become significant (as would be the case for an HRL maser).

For a uniform distribution of the emission measure, the free-free spectral index is $\alpha_{\text{ff}} \approx 2$ (optically thick) in lower ν , and $\alpha_{\text{ff}} \approx -0.1$ (optically thin) in higher ν , with a relatively narrow transition frequency range. The observed fluxes in VLA bands show consistent spectral indices between 0 and 2 for a quite wide frequency range, which requires a nonuniform distribution of the emission measure (and electron density). For simplicity, we assume the emitting region projected on the plane of sky is a circular disk with an outer radius of r_{out} , and the emission measure follows a power-law dependence on the radius r ,

$$\text{EM}(r) = \text{EM}_{10\text{au}} \left(\frac{r}{10 \text{ au}} \right)^{-\rho_{\text{EM}}}. \quad (\text{A12})$$

We also assume the disk has an inner radius of r_{in} to avoid singularity. Then we have the free-free and H30 α fluxes as

$$\left(\frac{S_{\nu,\text{ff}}}{\text{Jy}} \right) = 4.534 \times 10^{-10} \left(\frac{\nu}{\text{GHz}} \right)^2 \left(\frac{d}{\text{kpc}} \right)^{-2} \times \left(\frac{T_e}{\text{K}} \right) \int_{R_{\text{in}}}^{R_{\text{out}}} (1 - e^{-\tau_{\text{ff}}}) R dR, \quad (\text{A13})$$

and

$$\left(\frac{S_{\text{H30}\alpha}}{\text{Jy km s}^{-1}} \right) = 6.445 \times 10^{-5} \left(\frac{d}{\text{kpc}} \right)^{-2} \left(\frac{T_e}{\text{K}} \right)^{-3/2} \times \left(\frac{\text{EM}_{10\text{au}}}{\text{pc cm}^{-6}} \right) \int_{R_{\text{in}}}^{R_{\text{out}}} e^{-\tau_{\text{ff}}} R^{1-\rho_{\text{EM}}} dR, \quad (\text{A14})$$

where $R = r/10$ au, $R_{\text{in}} = r_{\text{in}}/10$ au, $R_{\text{out}} = r_{\text{out}}/10$ au, and τ_{ff} is given by Equation (A1). These are the observed quantities we fit with the model.

To further reduce the free parameters in the model, we adopt $r_{\text{in}} = 10 R_{\odot}$ (0.05 au), and $r_{\text{out}} = 50$ au. The inner radius of $10 R_{\odot}$ is a typical stellar radius for massive protostars reaching the main sequence (e.g., Zhang & Tan 2018). The outer radius of 50 au is roughly consistent with the observation (see Figure 6). Therefore, we have three free parameters in this model, the electron temperature of the ionized gas (T_e), the emission measure at the radius of 10 au ($\text{EM}_{10\text{au}}$), and the power-law index of the emission measure distribution ρ_{EM} . We expect the electron density distribution has a power-law form $n_e \sim r^{-\rho_{n_e}}$ with $1.5 \leq \rho_{n_e} \leq 2$. The power-law index of -1.5 for the electron density corresponds to the case of the surface of a photoionized disk around a massive forming star (Tanaka et al. 2013). The power-law index of -2 of the electron density corresponds to the case of an expansion flow of the ionized gas with constant velocity. The emission measure is then $\text{EM} \sim n_e^2(r)l$, where l is the line-of-sight length scale of the ionized region. As a first-order estimate, we assume $l \propto r$ and $\text{EM} \sim n_e^2(r)r \sim r^{1-2\rho_{n_e}}$. Therefore, we limit the power-law index of the emission measure distribution to the range of $2 \leq \rho_{\text{EM}} \leq 3$ in the fitting.

To find the best-fit model, we compare the model free-free continuum flux densities (Equation (A13)) to the continuum fluxes observed in VLA bands, and compare the model H30 α flux integrated over velocity and space to the observed value from the ALMA observation. For each model, we calculate the test statistics χ_{ff}^2 and $\chi_{\text{H30}\alpha}^2$ as

$$\chi_{\text{ff}}^2 = \sum \frac{(S_{\nu,\text{ff,mod}} - S_{\nu,\text{ff,obs}})^2}{\sigma_{\nu,\text{ff,obs}}^2},$$

$$\chi_{\text{H30}\alpha}^2 = \frac{(S_{\text{H30}\alpha,\text{mod}} - S_{\text{H30}\alpha,\text{obs}})^2}{\sigma_{\text{H30}\alpha,\text{obs}}^2}, \quad (\text{A15})$$

where the summation of χ_{ff}^2 is for all the VLA bands. Then, we determine the best-fit model by minimizing the value of $\chi^2 = (\chi_{\text{ff}}^2 + \chi_{\text{H30}\alpha}^2)/N$, where N is the total number of data points (including continuum and H30 α line) used in fitting. Note that the ALMA 1.3 mm continuum is not used for fitting the free-free emission, as it usually includes significant dust emission.

If the H30 α line has a non-LTE maser component (such as in source 3), we use the observed H30 α flux as an upper limit. If the H30 α line is not detected (such as in source 1), we use the 3σ level in the integrated map as an upper limit. If the observed H30 α and ALMA 1.3 mm continuum fluxes indicate strong dust continuum contributions even in VLA bands, we also include the dust component following

$$S_{\nu,\text{dust}} = S_{234\text{GHz,dust}} \left(\frac{\nu}{234 \text{ GHz}} \right)^{\alpha_{\text{dust}}}, \quad (\text{A16})$$

and fit all the continuum fluxes (VLA and ALMA) with $S_{\nu} = S_{\nu,\text{dust}} + S_{\nu,\text{ff}}$.

From the derived properties, we further estimate the ionizing photon rate by balancing the rates of recombination and photoionization, following the method by Schmiedeke et al. (2016),

$$\dot{N}_i = \int n_e^2 (\beta - \beta_1) dV = d^2 \int \text{EM} (\beta - \beta_1) d\Omega, \quad (\text{A17})$$







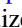


where β and β_1 are the rate coefficients for the recombination to all levels and to the ground state, i.e.,

$$\beta - \beta_1 = 4.1 \times 10^{-10} \text{ cm}^3 \text{ s}^{-1} \left(\frac{T_e}{\text{K}} \right)^{-0.8}. \quad (\text{A18})$$

From our assumptions on the emission measure distribution, we obtain the ionizing photon rate of

$$\dot{N}_i = 1.1 \times 10^{45} \text{ s}^{-1} \left(\frac{T_e}{10^4 \text{ K}} \right)^{-0.8} \times \left(\frac{\text{EM}_{10\text{au}}}{10^{10} \text{ pc cm}^{-6}} \right) \int_{R_{\text{in}}}^{R_{\text{out}}} R^{1-\rho_{\text{EM}}} dR. \quad (\text{A19})$$

ORCID iDs

Yichen Zhang  <https://orcid.org/0000-0001-7511-0034>
 Kei E. I. Tanaka  <https://orcid.org/0000-0002-6907-0926>
 Jonathan C. Tan  <https://orcid.org/0000-0002-3389-9142>
 Yao-Lun Yang  <https://orcid.org/0000-0001-8227-2816>
 Maria T. Beltrán  <https://orcid.org/0000-0003-3315-5626>
 Nami Sakai  <https://orcid.org/0000-0002-3297-4497>
 James M. De Buizer  <https://orcid.org/0000-0001-7378-4430>
 Viviana Rosero  <https://orcid.org/0000-0001-8596-1756>
 Rubén Fedriani  <https://orcid.org/0000-0003-4040-4934>

References

- Allison, R. J., Goodwin, S. P., Parker, R. J., et al. 2009, *MNRAS*, 395, 1449
 Anglada, G., Rodríguez, L. F., & Carrasco-González, C. 2018, *A&ARv*, 26, 3
 Bae, J., & Zhu, Z. 2018, *ApJ*, 859, 119
 Beltrán, M. T., Cesaroni, R., Moscadelli, L., et al. 2016, *A&A*, 593, A49
 Beltrán, M. T., & de Wit, W. J. 2016, *A&ARv*, 24, 6
 Beuther, H., Mottram, J. C., Ahmadi, A., et al. 2018, *A&A*, 617, A100
 Birks, J. R., Fuller, G. A., & Gibb, A. G. 2006, *A&A*, 458, 181
 Bonnell, I. A., Bate, M. R., Clarke, C. J., & Pringle, J. E. 2001, *MNRAS*, 323, 785
 Bonnell, I. A., & Davies, M. B. 1998, *MNRAS*, 295, 691
 Busquet, G., Girart, J. M., Estalella, R., et al. 2019, *A&A*, 623, L8
 Caratti o Garatti, A., Stecklum, B., Linz, H., et al. 2015, *A&A*, 573, A82
 Cartwright, A., & Whitworth, A. P. 2004, *MNRAS*, 348, 589
 Churchwell, E. 2002, *ARAA*, 40, 27
 Davies, B., Hoare, M. G., Lumsden, S. L., et al. 2011, *MNRAS*, 416, 972
 De Buizer, J. M. 2006, *ApJL*, 642, L57
 De Buizer, J. M., Liu, M., Tan, J. C., Zhang, Y., et al. 2017, *ApJ*, 843, 33
 Fedriani, R., Caratti o Garatti, A., Purser, S. J. D., et al. 2019, *NatCo*, 10, 3630
 Forgan, D. H., Ilee, J. D., & Meru, F. 2018, *ApJL*, 860, L5
 Gibb, A. G., Hoare, M. G., Little, L. T., & Wright, M. C. H. 2003, *MNRAS*, 339, 1011
 Ginsburg, A., Bally, J., Goddi, C., et al. 2018, *ApJ*, 860, 119
 Goddi, C., Ginsburg, A., Maud, L. T., et al. 2020, *ApJ*, 905, 25
 Guzman, A. E., Sanhueza, P., Zapata, L., et al. 2020, *ApJ*, 904, 77
 Haemmerlé, L., & Peters, T. 2016, *MNRAS*, 458, 3299
 Hagberg, A. A., Schult, D. A., & Swart, P. J. 2008, in Proc. of the VII Python in Science Conf. (SciPy2008), ed. G. Varoquaux, T. Vaught, & J. Millman, 11, <http://conference.scipy.org/proceedings/SciPy2008>
 Hanawa, T., Sakai, N., & Yamamoto, S. 2022, *ApJ*, 932, 122
 Heaton, B. D., & Little, L. T. 1988, *A&A*, 195, 193
 Hoare, M. G., Kurtz, S. E., Lizano, S., Keto, E., & Hofner, P. 2007, in Protostars and Planets V, ed. B. Reipurth, D. Jewitt, & K. Keil (Tucson, AZ: Univ. Arizona Press), 181
 Hollenbach, D., Johnstone, D., Lizano, S., & Shu, F. 1994, *ApJ*, 428, 654
 Hosokawa, T., & Omukai, K. 2009, *ApJ*, 691, 823
 Hosokawa, T., Yorke, H. W., & Omukai, K. 2010, *ApJ*, 721, 478

- Huang, J., Andrews, S. M., Pefez, L. M., et al. 2018, *ApJL*, **869**, L43
- Ilee, J. D., Cyganowski, C. J., Brogan, C. L., et al. 2018, *ApJL*, **869**, L24
- Ilee, J. D., Cyganowski, C. J., Nazari, P., et al. 2016, *MNRAS*, **462**, 4386
- Jiménez-Serra, I., Báez-Rubio, A., Martín-Pintado, J., et al. 2020, *ApJL*, **897**, L33
- Jiménez-Serra, I., Báez-Rubio, A., Rivilla, V. M., et al. 2013, *ApJL*, **764**, L4
- Johnston, K. G., Hoare, M. G., Beuther, H., et al. 2020, *A&A*, **634**, L11
- Johnston, K. G., Robitaille, T. P., Beuther, H., et al. 2015, *ApJL*, **813**, L19
- Keto, E. 2002, *ApJ*, **580**, 980
- Keto, E. 2003, *ApJ*, **599**, 1196
- Kraus, S., Kluska, J., Kreplin, A., et al. 2017, *ApJL*, **835**, L5
- Kruskal, J. 1956, *Proc. Am. Math. Soc.*, **7**, 48
- Kuffmeier, M., Calcutt, H., & Kristensen, L. E. 2019, *A&A*, **628**, A112
- Kuiper, R., & Hosokawa, T. 2018, *A&A*, **616**, A101
- Kurtovic, N. T., Pérez, L. M., Benisty, M., et al. 2018, *ApJL*, **869**, L44
- Liu, H. B. 2017, *A&A*, **597**, A70
- Martín-Pintado, J., Bachiller, R., Thum, C., & Walmsley, M. 1989, *A&A*, **215**, L13
- Maud, L. T., Cesaroni, R., Kumar, M. S. N., et al. 2018, *A&A*, **620**, 31
- Maud, L. T., Cesaroni, R., Kumar, M. S. N., et al. 2019, *A&A*, **627**, L6
- McKee, C. F., & Tan, J. C. 2003, *ApJ*, **585**, 850
- McMullin, J. P., Waters, B., Schiebel, D., Young, W., & Golap, K. 2007, in *ASP Conf. Ser. 376, Astronomical Data Analysis Software and Systems XVI*, ed. R. A. Shaw, F. Hill, & D. J. Bell (San Francisco, CA: ASP), 127
- Moscadelli, L., Cesaroni, R., Beltrán, M. T., & Rivilla, V. M. 2021, *A&A*, **650**, 142
- Moser, E., Liu, M., Tan, J. C., et al. 2020, *ApJ*, **897**, 136
- Motogi, K., Hirota, T., Machida, M., et al. 2019, *ApJL*, **877**, L25
- Motte, F., Bontemps, S., & Louvet, F. 2018, *ARA&A*, **56**, 41
- Mottram, J. C., Hoare, M. G., Davies, B., et al. 2011, *ApJL*, **730**, L33
- Müller, H. S. P., Schlöder, F., Stutzki, J., & Winnewisser, G. 2005, *JMoSt*, **742**, 215
- Ossenkopf, V., & Henning, T. 1994, *A&A*, **291**, 943
- Oya, Y., Sakai, N., López-Sepulcre, A., et al. 2016, *ApJ*, **824**, 88
- Palau, A., Fuente, A., Girart, J. M., et al. 2013, *ApJ*, **762**, 120
- Peters, T., Banerjee, R., Klessen, R. S., et al. 2010, *ApJ*, **711**, 1017
- Pineda, J. E., Segura-Cox, D., Casselli, P., et al. 2020, *NatAs*, **4**, 1158
- Plunkett, A. L., Fernández-López, M., Arce, H. G., et al. 2018, *A&A*, **615**, A9
- Qiu, K., Zhang, Q., Menten, K. M., Liu, H. B., & Tang, Y.-W. 2013, *ApJ*, **779**, 182
- Sakai, N., Sakai, T., Hirota, T., et al. 2014a, *Natur*, **507**, 78
- Sánchez-Monge, Á., Beltrán, M. T., Cesaroni, R., et al. 2014, *A&A*, **569**, A11
- Sánchez-Monge, Á., Cesaroni, R., Beltrán, M. T., et al. 2013, *A&A*, **552**, L10
- Schmiedeke, A., Schilke, P., Möller, Th., et al. 2016, *A&A*, **588**, A143
- Sewilo, M., Churchwell, E., Kurtz, S., et al. 2004, *ApJ*, **605**, 285
- Tan, J. C., Beltrán, M. T., Caselli, P., et al. 2014, in *Protostars and Planets VI*, ed. H. Beuther et al. (Tucson, AZ: Univ. Arizona Press), 149
- Tanaka, K. E. I., Nakamoto, T., & Omukai, K. 2013, *ApJ*, **773**, 155
- Tanaka, K. E. I., Tan, J. C., & Zhang, Y. 2016, *ApJ*, **818**, 52
- Tanaka, K. E. I., Tan, J. C., & Zhang, Y. 2017, *ApJ*, **835**, 32
- Tanaka, K. E. I., Zhang, Y., Hirota, T., et al. 2020, *ApJL*, **900**, L2
- Tobin, J. J., Chandler, C. J., Wilner, D. J., et al. 2013, *ApJ*, **779**, 93
- Tychoniec, Ł., Tobin, J. J., Karska, A., et al. 2018, *ApJS*, **238**, 19
- Wang, P., Li, Z.-Y., Abel, T., & Nakamura, F. 2010, *ApJ*, **709**, 27
- Wilson, T. L., Rohlfs, K., & Hüttemeister, S. 2013, *Tools of Radio Astronomy* (6th edn.; Berlin: Springer), doi:10.1007/978-3-642-39950-3
- Wu, Y. W., Sato, M., Reid, M. J., et al. 2014, *A&A*, **566**, A17
- Zhang, B., Zheng, X. W., Reid, M. J., et al. 2009, *ApJ*, **693**, 419
- Zhang, Q., Claus, B., Watson, L., & Moran, J. 2017, *ApJ*, **837**, 53
- Zhang, Y., & Tan, J. C. 2018, *ApJ*, **853**, 18
- Zhang, Y., Tan, J. C., De Buizer, J. M., et al. 2013, *ApJ*, **767**, 58
- Zhang, Y., Tan, J. C., & Hosokawa, T. 2014, *ApJ*, **788**, 166
- Zhang, Y., Tan, J. C., & Sakai, N. 2019a, *ApJ*, **873**, 73
- Zhang, Y., Tan, J. C., Tanaka, K. E. I., et al. 2019b, *NatAs*, **3**, 517
- Zhang, Y., Tanaka, K. E. I., Rosero, V., et al. 2019c, *ApJL*, **886**, L4
- Zhu, Z., Dong, R., Stone, J. M., & Rafikov, R. R. 2015, *ApJ*, **813**, 88